Investigation of crystal structure, electrical and dielectric response of Ga3+ substituted Sr–Ni Y-type hexaferrites as a suitable material for high frequency applications

Article *in* Ceramics International · April 2023

DOI: 10.1016/j.ceramint.2023.03.239

8 authors, including:

Muhammad Arshad
The Islamia University of Bahawalpur
5 PUBLICATIONS **52** CITATIONS
SEE PROFILE

Muhammad Azhar Khan
The Islamia University of Bahawalpur
309 PUBLICATIONS **8,330** CITATIONS
SEE PROFILE

Muhammad Imran Arshad
Government College University Faisalabad, Punjab Pakistan
135 PUBLICATIONS **1,916** CITATIONS
SEE PROFILE

Hind Albalawi
Princess Nora bint Abdul Rahman University
101 PUBLICATIONS **977** CITATIONS
SEE PROFILE

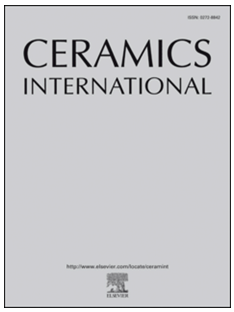

Investigation of crystal structure, electrical and dielectric response of Ga^{3+} substituted Sr–Ni Y-type hexaferrites as a suitable material for high frequency applications

Muhammad Arshad, Muhammad Azhar Khan, Raqiqa Tur Rasool, Muhammad Imran Arshad, Hind Albalawi, Hisham S.M. Abd-Rabboh, Jolly Jacob, H.M. Noor ul Huda Khan Asghar

PII: S0272-8842(23)00839-8

DOI: https://doi.org/10.1016/j.ceramint.2023.03.239

Reference: CERI 36196

To appear in: *Ceramics International*

Received Date: 18 January 2023

Revised Date: 12 March 2023

Accepted Date: 25 March 2023

Please cite this article as: M. Arshad, M.A. Khan, R.T. Rasool, M.I. Arshad, H. Albalawi, H.S.M. Abd-Rabboh, J. Jacob, H.M.N.u.H.K. Asghar, Investigation of crystal structure, electrical and dielectric response of Ga^{3+} substituted Sr–Ni Y-type hexaferrites as a suitable material for high frequency applications, *Ceramics International* (2023), doi: https://doi.org/10.1016/j.ceramint.2023.03.239.

Investigation of Crystal Structure, Electrical and Dielectric Response of Ga^{3+} Substituted Sr-Ni Y-Type Hexaferrites as a Suitable Material for High Frequency Applications

Muhammad Arshad*[a] Muhammad Azhar Khan*[a], Raqiqa Tur Rasool*[b], Muhammad Imran Arshad[c], Hind Albalawi[d], Hisham S. M. Abd-Rabboh[e,f], Jolly Jacob[g], H. M. Noor ul Huda Khan Asghar[h]

[a]*Institute of Physics, The Islamia University of Bahawalpur, Bahawalpur-63100, Pakistan*
[b]*Department of Physics, Zhejiang Normal University, Jinhua, Zhejiang321004, China*
[c]*Department of Physics, Government College University, Faisalabad,38000, Pakistan*
[d]*Department of Physics, College of Science, Princess Nourah bint Abdulrehman University (PNU), P.O. Box 84428, Riyadh 11671, Saudi Arabia*
[e]*Chemistry Department, Faculty of Science, King Khalid University, P.O. Box 9004, Abha 61413, Saudi Arabia*
[f]*Department of Chemistry, Faculty of Science, Ain Shams University, Abbassia, Cairo 11566, Egypt*
[g]*College of Arts and Science, Abu Dhabi University UAE*
[h]*Department of Physics, Balochistan University of Information Technology, Engineering & Management Sciences, Quetta, 87300, Pakistan*

*Corresponding authors: Muhammad.arshadiub@gmail.com, azhar.khan@iub.edu.pk

**Corresponding author: ra_chem@yahoo.com

Abstract

Technology important ferrites ceramic $Sr_2Ni_2Ga_xFe_{12-x}O_{22}$ (x=0.00, 0.2, 0.4, 0.6, and 0.8) samples were produced using sol-gel auto combustion route. Structural, electrical, dielectric, and magnetic parameters were identified by substituting Ga^{3+} at the Fe^{3+} site. It was recognized that an increase of Ga^{3+} content in ($Sr_2Ni_2Ga_xFe_{12-x}O_{22}$) ceramic samples first decreased, then increased lattice parameters, and the density of samples was observed. This is because of the ionic radii and atomic weight of Ga^{3+} and Fe^{3+} cations. FTIR spectra show two characteristic absorption bands at 444-513 cm^{-1} caused by metal-oxygen vibrations. Due to the contribution of smaller grains of samples, the higher values of resistivity were observed, which vary from 3.78×10^{10} (Ω cm) to 1.13×10^{11} (Ω cm) by the substitution of Ga^{3+} ions at the octahedral site. The activation energy was measured between 0.20-0.61 eV. The dielectric response of Ga^{3+} substituted ferrite ceramic samples were studied in the 1 MHz-6 GHz frequency region. The

Maxwell-Wagner bilayer model studied the effect of polarization with applied frequency on dielectric parameters. With the substitution of Ga^{3+}, minimal losses in the range 0.34-0.44, about 6 GHz, and a high Q-value of about 10,000 were observed for each sample. In impedance spectroscopy analysis Cole-Cole plots confirm that the dielectric response is because of the influence of grain boundaries. The substitution of Ga^{3+} enhances saturation magnetization (68.20-71.78 emu/g) while coercivity decreases (655.86-507.86 Oe). In the present finding, the low dielectric loss, moderate permittivity, high value of the Quality factor, and very high value of resistivity of about 1.13×10^{11} that reduces the eddy current losses suggested that these materials are appropriate candidates for many high-frequency applications such as multilayer chip inductor, dielectric resonators, power applications, and microwave devices.

Keywords: XRD; Sr-Ni-Ga-Fe-O System; FTIR; Resistivity; High-frequency Applications.

1. Introduction

Ferrites are a unique group of oxides with excellent magnetic characteristics which have been studied and used in several fields over the past 50 years [1]. Due to their curious electrical and dielectric properties, ferrites are very important for the electronic industry [2]. Ferrites in the nanocrystalline form are used in various novel technologies, including magnetically guided medication delivery, magnetic resonance imaging (MRI), catalysts, humidity and gas sensors, magnetic fluids, MLCI, and more [3]. These uses are based on the fundamental characteristics of ferrites, which include large saturation magnetization, high electrical resistivity, negligible electrical losses, and excellent chemical stability [1]. Spinel, garnets, orthoferrites, and hexaferrites are the four crystallographic classes of ferrites. Among these categories, hexagonal ferrites are useful for MW applications [4]. Went and colleagues [5] introduced the hexagonal phase in 1952; Jonker et al. followed in 1956 [6]. A series of closely related compounds with hexagonal and rhombohedral symmetry is known as hexagonal ferrites. Unlike garnet and spinel ferrites, hexagonal ferrites show many crystal structures [7]. These ferrites can be divided into seven categories based on their chemical composition and crystal structure: M, W, Y, X, Z, U, and R-type hexaferrites [8]. The formula for the crystal structure of Y-type hexagonal ferrite is $Ba_2Me_2Fe_{12}O_{22}$. Only metal ions occupy the tetrahedral (A) and octahedral (B) positions. Four

ions are in tetrahedral positions in Y-type ceramic material, and ten ions are found in octahedral sites in one formula unit, $Ba_2Me_2Fe_{12}O_{22}$ [9]. The interior layers of two R blocks can be linked to form a T block. Octahedral ions are stacked one on the other, and a second pair corresponding to two octahedral ions are transferred from the adjacent barium layer. Three octahedral ions are found in this way, stacked one over the other. The metal ion is short near the cores of the other oxygen tetrahedrons. S blocks are rotated concerning one another because T blocks do not include a mirror plane [10-13].

The researchers are synthesizing new ceramic materials with enhanced and outstanding electrical and dielectric properties in the GHz frequency range. Sr-based hexaferrites are excellent materials owing to their high electrical resistivity and semi-conductive nature to use them through the whole GHz range. Modern electronic device technology demands high resistivity (~ 10^{11} Ω cm) to reduce eddy current losses, soft magnetic nature, and high cut-off frequency at the GHz range. Thus Y-type hexagonal ferrite ceramics are attractive to researchers due to their wide range of applications [14, 15].

Due to their planar magnetic anisotropy, soft Y-type ferroxplana hexagonal ferrites display high cut-off frequency in the gigahertz range. Electrical and dielectric features of Ni_2Y hexaferrites were significantly altered when we substituted cations at the Fe site. Faiza Aen et al. [16] investigate the Ga^{3+} substitution effect on the electromagnetic properties of W-type ferrites. Rehman et al. [17] study the Cr^{3+} substituted W-type ferrites; as the substitution level increase, eddy current losses decreases, which is highly desirable for high-frequency applications devices. Akthar et al. [18] synthesized Ga^{3+} substituted Yttrium iron garnet.

In the present work, trivalent Ga^{3+} metal ions are selected to substitute at the iron site of Ni_2Y hexaferrite with chemical formula $Sr_2Ni_2Ga_xFe_{12-x}O_{22}$ ($0.00 \leq x \leq 0.8$ and $\Delta x = 0.2$) manufactured by sol-gel route. The main advantage of this method is cheaper; nanoscale formation and low annealing temperature were required. The reason for choosing Ga^{3+} at the iron site is that the ionic radii of Ga^{3+}=0.62 Å are comparable to Fe^{3+}= 0.64 Å, and the resistivity of Ga is more than iron. In the present work, the substitution of Ga^{3+} at the octahedral site limits the hopping of electrons; consequently, electrical resistivity increases, which decreases the eddy current losses, and optimized dielectric properties were observed to suggest that these samples

are favorable for many high-frequency applications which is the requirement of modern electronic devices.

2. Experimental details

2.1. Chemicals and reagents

Initially, the following metal nitrates were used for the synthesis of $Sr_2Ni_2Ga_xFe_{12-x}O_{22}$ (x=0.00, 0.2, 0.4, 0.6 and 0.8): Strontium nitrate ($Sr(NO_3)_2$), Nickel nitrate 6-hydrate ($Ni(NO_3)_2.6H_2O$), Gallium nitrate hydrate ($Ga(NO_3)_3.\ xH_2O$), Iron nitrate nano-hydrate ($Fe(NO_3)_2\ .9H_2O$) and as a chelating agent citric acid ($C_6H_8O_7.\ 1H_2O$). Finally, deionized water was employed as the solvent. All the necessary metal nitrates and chemicals were utilized as they were purchased without purification.

2.2. Synthesis procedure of $Sr_2Ni_2Ga_xFe_{12-x}O_{22}$ ($0.0 \leq x \leq 0.8$ and $\Delta x = 0.2$) hexaferrites

Single phase Ga^{3+} substituted Sr-Ni-Y-type hexaferrites with chemical composition $Sr_2Ni_2Ga_xFe_{12-x}O_{22}$ ($0.0 \leq x \leq 0.8$ and $\Delta x = 0.2$) were prepared by environmentally friendly and low-cost sol-gel auto-ignition method. Firstly, the required amounts of metal nitrate (powders) and citric acid (chelating agent) were weighed in stoichiometric ratios and dissolved in separate beakers containing the deionized water necessary. Further, these metal nitrate solutions were stirred for 5-6 minutes to acquire uniform solutions. These solutions were mixed in five different clean beakers according to their desired stoichiometric ratios. They were kept on magnetic stirrers for continuous stirring and heating up to 45 ˚C by fixing the Temperature. By adding a chelating agent, the pH of the solutions was between 10 – 12, which was reduced to 7 by pouring a concentrated solution of ammonium hydroxide (30-33% NH_3) in a dropwise manner. With the addition of ammonia, the color of the solutions was changed, and the pH was maintained at 7.

Further, increased Temperature of up to 80 – 85 ˚C of magnetic hot plates and constant stirring for about 5-6 h to produce gel by the evaporation of water. The viscous gel was

automatically burnt and transformed into fluffy texture ash. After 15 minutes of grinding in a pestle and mortar, the fluffy precursor ash was converted to a fine powder. Finally, it was sintered in a digitally controlled box furnace at 1423 K for 5.5 h then sintered powders were ground to obtain a fine powder. For pellets formation, polyvinyl alcohol was used as a binder mixed in a sintered sample, then applying the pressure of 30 KN via hydraulic press for 3-4 minutes to form a circular pellet of 7mm diameter. These pellets were again calcined at 200 ˚C for 30 minutes to remove the organic binder. For good ohmic contact, the silver paste was painted on the pellets.

2.3. Characterization techniques

To investigate the required phase formation and structural properties of these fabricated materials, they were confirmed by an XRD diffractometer (Bruker D8) using (Cu-Kα) as a radiation source in the angle range of 20˚-70˚. FTIR analysis was done by KBr pellet method technique in wave numbers 400-4000 cm^{-1} range using Bruker spectrometer. A two-point probe method measured temperature-dependent DC resistivity up to 400 ˚C using the Keithley electrometer model 2401 source meter. This study aims to learn more about the dielectric and impedance response of the fabricated samples from 1 MHz to 6 GHz. “Epsilometer R60 VNA” (Copper Mountain Technology) was used in this study. SEM analysis was used to understand the surface morphology of the synthesized samples. The magnetic behavior of Ga^{3+} substituted specimens was investigated through VSM 7400 at room temperature.

3. Results and discussion

3.1. Structural analysis

XRD patterns of pure and Ga^{3+} substituted Sr-Ni Y-type ceramic ferrites are shown in Fig. 1. The observed sharp peaks in the XRD patterns confirm the phase purity and crystallinity of the fabricated samples. Identified peaks are well matched according to Y-type hexaferrites ICDD standard pattern with reference code (01-073-2035). These findings demonstrate that a pure single phase of Y-type hexaferrite materials formed using the sol-gel auto-combustion technique after only 5.5 hours of annealing at 1150 °C. In the developed samples, the peaks were shifted slightly in the direction of higher angle values by substitution of Ga^{3+} cations; this

shifting of peaks was associated with the difference in ionic radius of Ga^{3+} cation (0.62 Å) as compared to Fe^{3+} cation (0.64 Å) [19, 20]. The variation in d-spacing and decline in D (grain size) was observed caused by the shifting of peaks towards the higher angle values [17]. The lattice parameters a (Å), c (Å), and V_{cell} were calculated by using the following relations [21, 22].

$$\frac{1}{d_{hkl}^2} = \frac{4}{3}\left[\frac{h^2+hk+k^2}{a^2}\right] + \frac{l^2}{c^2} \quad (1)$$

$$V_{cell} = \frac{\sqrt{3}}{2} a^2 c \quad (2)$$

Where d signifies the distance between two successive planes and hkl indicates the Miller indices correspondingly [23-25]. It was calculated that "a," "c," and V_{cell} decreased by increasing the content of Ga^{3+}, as presented in Table 1 and figure 2. This is due to replacing Ga^{3+} (smaller ionic) cations instead of Fe^{3+} (larger ionic) cations. The decrease in unit V_{cell} was observed caused by the reduction in lattice parameters via the substitution content. The c/a ratio of these fabricated ferrites was calculated between 7.39 to 7.49, which confirms that the synthesized samples belong to Y-type hexagonal ferrite [26]. The variation in c/a value and unit cell volume with substitution content of Ga^{3+} is presented in Fig. 3. The crystallite size of these investigated ferrites depends on angle θ and FWHM (β), which was determined from the following relation;

$$D = \frac{K\lambda}{\beta Cos\theta} \quad (3)$$

The values of (D) of these synthesized ceramic samples were calculated in 34- 41 nm, which approves that fabricated samples are in the nano range. The substitution effect of Ga^{3+} on the crystallite size and d-spacing is exposed in Fig. 4.

Some important terms such as D_x, D_b, and P (%) were calculated using the relation shown in Fig. 5 [27] for the physical characteristics of these synthesized ferrite materials.

$$D_x = \frac{ZM}{N_A V_{cell}} \quad (4)$$

$$D_b = \frac{m}{\pi r^2 h} \quad (5)$$

$$P\ (\%) = \left(1 - \frac{\rho_b}{\rho_x}\right) \times 100 \quad (6)$$

X-ray density (D_x) of the fabricated ferrite nano-materials was calculated from Eq. (4) [28], which showed that D_x was directly related to the molecular weight of ferrite ceramic samples and inversely related to the unit V_{cell}. The molecular weight of substituted (Ga) cations is greater than the host (Fe) ions. So in X-ray density, a non-linearly increasing trend was seen with Ga substitutions [29].

To check the quality of the fabricated samples, we calculate the porosity of the samples, which were affected by annealing temperature, synthesis route, and Ga3+ content. Bulk density (D_b) was measured at 3.21 g/cm^3 to 3.39 g/cm^3, which is always less than D_x by the occurrence of pores as they originated during the annealing of ceramic samples. The present investigation calculated porosity at 37.15 % to 32.74 %. Hence the ceramic samples were densified by the Ga^{3+} substitution content [30].

To investigate the variation in some other critical mechanical factors such as microstrain (ε), specific surface area (S) [31], stacking fault co-efficient (α) and dislocation density (δ) were measured from the XRD analysis by equations (7) to (10). Their corresponding values are presented in Table 1. Figure 6 demonstrates the correlation between these factors and substitution content (x).

$$S = \frac{6000}{(D_x \times D)} \quad (7)$$

$$\varepsilon = \frac{\beta}{4\tan\theta} \quad (8)$$

$$\delta = \frac{1}{D^2} \quad (9)$$

$$\alpha = \frac{2\pi^2}{45\sqrt{3}}\left(\frac{\Delta 2\theta}{\tan\theta}\right) \quad (10)$$

As determined by microstrain, crystal deformation and defects in Ga^{3+} substituted Y-type hexagonal ferrites resulted from substituting Ga metal cations for the host iron ions. These mechanical factors shift XRD peaks from their original positions [32]. The stacking fault co-

efficient was accountable for explaining the planar defects in the crystal lattice, while dislocation density was responsible for presenting the linear defects.

3.2. FTIR analysis

Fig. 7 shows the FTIR spectra of $Sr_2Ni_2Ga_xFe_{12-x}O_{22}$ ($0.0 \leq x \leq 0.8$ and $\Delta x = 0.2$) Y-type Hexa-ferrites at room temperature were recorded in the range from 400-4000 cm^{-1} as this range gives vital information about phase, structural and chemical changes in the fabricated samples that produce during the annealing process. In the 400-600 cm^{-1} range, characteristic absorption bands identified the development of Sr-Ni Y-type hexaferrites, the standard features of spinel, and M-type hexagonal ferrites [10, 33, 34]. The two important bands were identified accurately at 444 and 513 cm^{-1}. This confirms the M-O stretching vibrations at the crystal lattice's tetrahedral (A site) and octahedral (B site). The first signature band that was observed at 444 cm^{-1} contributes stretching vibration of the metal-oxygen band at tetrahedral ($Fe\text{-}O_4$) sites, and the second signature band at 513 cm^{-1} confirms the stretching vibration of the metal-oxygen band at octahedral ($Fe\text{-}O_6$) sites [35, 36]. Significant variations were observed in absorption bands with the substitution of Ga^{3+}, which confirms the inclusion of Ga^{3+} into Y-type hexagonal ferrite crystal lattice. No bands were observed in the 3500 cm^{-1} range, which guarantees that the ceramic samples are water-free, the main advantage of the sol-gel method.

3.3. Electrical properties

One of their most notable characteristics is the DC electrical resistivity of ferrite ceramic materials. Typically, high resistivity is required for most electrical applications. DC electrical resistivity (ρ_{dc}) of these produced ceramic samples $Sr_2Ni_2Ga_xFe_{12-x}O_{22}$ ($0.0 \leq x \leq 0.8$ and $\Delta x = 0.2$) were determined through I-V measurement technique in the temperature range of 303-673 K using the pellets of definite dimensions. The silver paste was applied on pellets from the ohmic contact. DC electrical resistivity of under-investigated samples was examined by varying the substitution level and Temperature by considering the relation; $\rho = AR/L$, here A, R, and L are the area, resistance, and width of the circular pellets.

3.3.1. Temperature dependence of resistivity

The relationship between Temperature and the DC electrical resistivity was calculated in the range of 303-673 K.

$$\rho = \rho_{\circ} \exp (\Delta E/K_B T) \quad (11)$$

Resistivity at room temperature T is denoted by ρ, activation energy (ΔE) is given by the slope of the Arrhenius plot, and K_B is the Boltzmann constant [37]. Y-type polycrystalline hexagonal ferrite ceramic material displays semiconducting behavior with the rise in Temperature. They show high DC electrical resistivity at room temperature in the 10^9-10^{11} Ω cm [38, 39]. The room temperature DC electrical resistivity at 303 K is presented in Fig 8.

The change in the values of electrical resistivity of Ga^{3+} doped materials in the temperature range of 303-673 K is displayed in Fig. 9, confirming the semiconducting nature of fabricated materials and showing kink at that point. Initially, the value of resistivity increases with Temperature, then suddenly decreases with Temperature. This increase in resistivity at low temperatures is due to the hygroscopic nature of these synthesized materials because ferrite material quickly absorbs moisture from the surrounding atmosphere. The transition temperature after which the material becomes paramagnetic is called Curie temperature. Because of Temperature, thermal vibrations tend to disturb the orderliness of domains. Ferromagnetic materials preserve orderliness at some ordinary temperatures. Due to this reason, resistivity increases with Temperature in the ferromagnetic region. After that reduction in resistivity concerning Temperature in the paramagnetic region was observed, and many other researchers followed the same behavior and reported it in the literature [40]. Hence the decrease in resistivity values with Temperature illustrates the semiconducting behavior of Ga^{3+} doped Y-type hexagonal ferrites. Verwey's hopping conduction mechanism is used to understand the conductivity in ferrite ceramic materials [41, 42]. In manufactured $Sr_2Ni_2Ga_xFe_{12-x}O_{22}$ ($0.0 \leq x \leq 0.8$ and $\Delta x = 0.2$) Y-type hexaferrites, electronic conduction was attributed to the sharing of electrons between metal cations of the same element that were in different valence states. When electrons hop from one ion of the same element to another, the distance between the ions and the activation energy plays a role. According to this mechanism, the electronic conduction in synthesized $Sr_2Ni_2Ga_xFe_{12-x}O_{22}$ ($0.0 \leq x \leq 0.8$ and $\Delta x = 0.2$) Y-type hexaferrites was owing to the exchange of electrons between metal cations of the same elements available in different valence states. The hopping of electrons between ions of the same elements depends on the separation between these ions and the

activation energy. As we increase the Temperature, the charge carriers are thermally activated; they have sufficient power to overcome the hurdle; it also increases the drift mobility of charge carriers; as a result, the decline in resistivity with the rise in Temperature. In low-temperature ferromagnetic regions, the conduction is due to the jumping of electrons between ferric and ferrous ions, while in high-temperature regions, polarons are responsible for hopping [43-45].

3.3.2. Effect of Ga^{3+} content on DC resistivity (ρ_{DC})

Table 2 and Fig. 10 illustrate the impact of Ga^{3+} substitution on the dc electrical resistivity values obtained at 303 K. Which confirms that electrical resistivity enhances from 3.78×10^{10} (Ω cm) to 1.13×10^{11} (Ω cm) with increasing the substitution of Ga^{3+} at octahedral lattice sites. The highest resistivity value of 1.13×10^{11} (Ω cm) for the composition $Sr_2Ni_2Ga_{0.80}Fe_{11.20}O_{22}$ is obtained, and its comparison with already reported resistivity values is presented in Table 3. Furthermore, the DC electrical resistivity of Y-type ferrite ceramics was powerfully affected by many parameters such as microstructure, grain size, stoichiometric composition, grain boundary content, porosity, and crystal imperfection. For all of these parameters, porosity is mainly important because pores (air/vacuum) in ferrites materials act as insulators. Due to this reason, the existence of porosity increases the resistivity of ferrite materials. In the present work, the increase in resistivity was contributed by porosity with the substitution of Ga^{3+}, which increase the separation between grains, and as a result, charge carrier hopping decreases [17]. Ga contributed the other cause of to increase in resistivity is more resistive (270×10^{-9} Ω m) than Fe (96.1×10^{-9} Ω m). When Ga substitutes Fe, the resistivity of the fabricated material is improved, which was one of the chief objectives of the present investigation. The variation in log ρ with respect to substitution content (x) in the 313-673 K temperature range was displayed in Fig. 11. The resistivity shows random behavior up to 363 K temperature further as we increase the substitution of Ga^{3+}.resistivity also increases.

The conductivity in ferrite ceramic materials was understood by band theory or the hopping model of electrons. This describes the transfer of electrons between Fe^{2+}/Fe^{3+} ion pairs on the octahedral site. When we replace Fe^{3+} with Ga^{3+} cations at the octahedral site, fewer Fe^{3+} ions are available for hopping electrons between Fe^{2+}/Fe^{3+}; as a result, resistivity increases [44].

3.3.3. Activation energy (ΔE)

The activation energies for prepared $Sr_2Ni_2Ga_xFe_{12-x}O_{22}$ ($0.0 \leq x \leq 0.8$ and $\Delta x = 0.2$) Y-type ferrite ceramic materials were calculated from the relation:

$$\Delta E = 2.203 \times K_B \times 1000 \times slope \quad (12)$$

K_B is the Boltzmann constant its value is 8.02×10^{-5} (eV/K), and the slope was determined from the linear fit of the plot log ρ vs. 1000/T. ΔE (activation energy) for successfully hopping electrons from one metal ion to the next [46]. ΔE in Para and ferromagnetic region are presented in Table 2. The variation in ΔE (activation energy) is directly related to the substitution content of Ga^{3+}, as displayed in Fig. 12. The activation energy of the paramagnetic region is greater than the ferromagnetic region following the theory of Irkin and Turov. In the ferromagnetic region, the conduction is due to electrons hopping, so less energy is required compared to the paramagnetic region. In this region, the conduction is due to polaron, so more energy is required for polaron hopping compared to electron hopping. A high activation energy (ΔE) corresponds to a high resistivity (ρ) in a given material, and vice versa [47].

Ferrites were highly resistive materials and showed semiconductor behavior with Temperature due to the less availability of free charge carriers. The activation energy in ferrite ceramics relies on the mobility of charges rather than carrier concentration. The drift mobility μ_d of all Ga^{3+} substituted samples was calculated by using the relation [48]:

$$\mu_{d=1/ne\rho} \quad (13)$$

In the above equation, n, e symbolizes the number and charge of electrons. Value of charge carrier "n" found by the relation:

$$n = N_A d_b P_{Fe} / M \quad (14)$$

In this relation M (molecular weight), d_b (bulk density), N_A (Avogadro's number), and P_{Fe} devote the number of iron atoms in the chemical composition. The values of drift mobility increased in the range 9.46×10^{-15} ($cm^2v^{-1}s^{-1}$) to 3.19×10^{-15} ($cm^2v^{-1}s^{-1}$) were tabulated in Table 2 and shown in Fig. 12. The Ga^{3+} substituted hexaferrites with high electrical resistivity illustrate the small value of drift mobility and vice versa [49-51].

3.4. Dielectric properties

The dielectric properties were essential to determine ferrite ceramic materials for many high-frequency applications, such as using them in integrated chip components. The dielectric properties of ferrite ceramic materials strongly depended on the applied frequency. They were influenced by many factors such as chemical composition, annealing temperature and time, occupation of cations on octahedral and tetrahedral lattice sites, and preparation method. Therefore the dielectric parameters were fundamental properties of interest for many high-frequency applications. Thus to improve the dielectric properties of hexaferrite ceramic materials, the necessary condition for that is maintaining low conductivity [13].

3.4.1. Dielectric constant (ε)

The permittivity or dielectric constant of $Sr_2Ni_2Ga_xFe_{12-x}O_{22}$ ($0.0 \leq x \leq 0.8$ and $\Delta x = 0.2$) Y-type hexagonal ferrites in the frequency of 1 MHz - 6 GHz range were calculated from pellets based on the equation given as

$$Dielectric\ constant = \varepsilon = \frac{Cd}{\varepsilon_{\circ}A} \quad (15)$$

In equation (15), C, A, and d represent the pellets' capacitance, area, and thickness, respectively. The permittivity of free space is $\varepsilon_{\circ}$. The dielectric constant behavior of synthesized $Sr_2Ni_2Ga_xFe_{12-x}O_{22}$ (x=0.00, 0.2, 0.4, 0.6, and 0.8) hexaferrites is shown in Fig. 13. Initially at the low-frequency region, the high value of permittivity is observed which suddenly decrease with applied frequency around 1 MHz, exhibit the ordinary behavior of ferrite ceramic samples with frequency due to dislocations, moisture, impurities, and voids were reported by many researchers [52]. Up to 2 GHz of applied frequency, the actual part of the permittivity increases significantly. Resonance peaks were found in the 2–4 GHz frequency band, where the dielectric constant is constant. The dielectric constant steadily rises with increasing frequency in the 4–6 GHz region. For x= 0.2 around 6 GHz, the dielectric constant is at its highest value of 2.70. The dielectric constant of Sr-Ni Y-type hexagonal ferrite grows more significant as the amount of Ga^{3+} in the material is increased. The electronic, ionic, dipolar, and interfacial polarization mechanisms all have a role in the frequency-dependent changes in the dielectric constant. The electronic polarization arises due to the shifting of the electronic cloud in the direction of the applied field [20]. The ionic polarization occurs due to ionic bonds between negative and positive ions of polycrystalline ferrite materials by the applied field. These two polarization processes required

normally high frequency (10^9 to 10^{12} Hz). The orientation polarization arises due to the alignment of dipoles in the direction of an applied field. The Maxwell-Wagner model was used to understand the interfacial polarization at the two-material interface and depends on the charge carrier conductivity in these two materials [53]. Polycrystalline ferrite ceramic samples contain electrically conducting grains by the regular arrangement of atoms broken at resistive thin grain boundaries. The accumulation of charges at resistive grain boundaries produces interfacial polarization. These accumulated charges at grain boundaries increase the interfacial polarizations, which enhances the dielectric constant. Some other factors are also responsible for the increase in interfacial polarization, i.e., oxygen vacancies, grain boundary defects, and local valence variations were the other reasons for the increase in dielectric constant [12].

Conduction in nanoscale ferrite ceramics is promoted by exchanging electrons among ferrous and ferric ions. In the present investigation, the increase in dielectric constant with Ga^{3+} substituted $Sr_2Ni_2Ga_xFe_{12-x}O_{22}$ ($0.0 \leq x \leq 0.8$ where $\Delta x = 0.2$) Y-type hexagonal ferrites is due to the site preference of Ga at the octahedral site. The highest value of permittivity was observed for Ga3+ substitution at x= 0.2. The comparison of dielectric results with the already reported results is listed in Table 4 [13, 54].

3.4.2. Dielectric loss (ε')

Fig. 14 illustrates the variation in ε' with applied frequency and substitution content of Ga^{3+}. The imaginary part of permittivity indicates the dissipation of energy due to the dominant conduction process in ferrite ceramic material was the hopping of electrons and the effect of different types of polarization mechanism that is produced with the application of frequency in the range of 1 MHz- 6 GHz [55]. In this study, the imaginary part of dielectric permittivity remains constant up to 1 GHz. After that, the values ε' increases with applied frequency up to 6 GHz. With increasing the substitution content of Ga^{3+}, the losses also increased. This enhancement in dielectric loss is due to different types of polarization mechanisms, the contribution of grain boundaries, the site occupied by cations at their respective sites, and the ionic radius of the substituted cations [56, 57].

3.4.3. Dielectric tan loss

Tangent loss of the fabricated Y-type polycrystalline materials is depicted in Fig. 15. The tan (δ) indicates the dissipation of electrical energy in ferrite ceramic materials due to various physical parameters such as electrical conduction, dielectric resonance, and dielectric relaxation. The dielectric losses originated due to the delay between the electric displacement vector and the applied electric field. In the present investigation tan (δ) increases with the applied frequency. The Maxwell-Wagner theory explains this rising trend of tan (δ). This observed tan (δ) behavior is like an imaginary part of dielectric loss as a function of applied frequency. Conduction in the low-frequency band (1 MHz-2 GHz) is primarily due to grain boundaries. Due to the resistive nature of grain boundaries, they operate as a hurdle for charge carriers, so a sufficient amount of energy is required for successful hopping. So in this region, tan (δ) remains constant. With more rise in frequency up to 6 GHz, the dielectric tangent loss enhanced, and some resonance peaks were observed in this due to matching the applied frequency with the hopping of electrons. The tan (δ) also increases with the substitution level of Ga^{3+}, which is greatest at x= 0.8. Other factors affecting the value of dielectric tangent loss are annealing Temperature, synthesis method, grain boundaries, porosity, dopant atoms, and dislocations.

3.4.4. AC conductivity

AC conductivity is associated with charge carrier movement and hopping in terms of Fe^{3+}/Fe^{2+} at the B site. So Verwey's hopping mechanism and mobility of charge carriers are responsible for the conduction process in polycrystalline ferrite magnetic materials, which can be calculated with the help of the following relation:

$$\sigma_{ac=2\pi f\varepsilon_{\circ}\varepsilon'=2\pi f\varepsilon_{\circ}\varepsilon(Tan\delta)} \quad (16)$$

The variation in AC conductivity versus frequency for the synthesized $Sr_2Ni_2Ga_xFe_{12-x}O_{22}$ ($0.0 \leq x \leq 0.8$ and $\Delta x = 0.2$) ferrites material is displayed in Fig. 16. There is a direct relation between applied field frequency and AC conductivity. AC conductivity is directly related to external field frequency, which enhances Verwey's hopping mechanism [30, 54]. This increasing behavior is well described by considering Maxwell-Wagner and Koop's theory. In light of these models, the microstructure of polycrystalline ferrite materials consists of conductive grains that are separated by resistive grain boundaries. The smaller value of σ_{ac} is due to grain boundaries' contribution in the low-frequency region. Because of the increased efficiency with which electrons can easily

hop between two adjacent lattice sites at high frequencies (up to 6 GHz), a significant value of σac is observed at this frequency range attributed to the presence of conductive grains. As we increase the doping level of Ga^{3+}, the σ_{ac} rises, and the maximum value at x=0.2 is observed.

3.4.5. Quality factor (Q)

Quality factor (Q) is reciprocal of tan(δ): Q = 1/ tan(δ) is recognized as a dissipation factor to evaluate the efficiency of electrical circuits in terms of their components such as an inductor, resistor or capacitor according to their bandwidth and losses. Y-type polycrystalline ferrite ceramics were very efficient materials to use in high-frequency applications because they exhibit very high resistivity values; due to this reason, the quality factor is significant to measure. The variation in quality factor concerning the substitution content of Ga^{3+} and field frequency is shown in Fig. 17. With the application of frequency, Q values increase up to 1 GHz. After that, it becomes decreasing, attains the constant value, and shows frequency-independent behavior. All the fabricated samples revealed optimized dielectric parameters such as high Q values and low dielectric losses. A very high Q value is observed between 10000-12000. If the Q value exceeds 1000, these materials were potentially used in high-frequency electronic devices such as high-frequency filters, resonators, and multilayer chip inductors [52].

3.4.6. Impedance spectroscopic studies

The effective and powerful technique to account for the electrical transport parameters of ferrite ceramic materials in 1 MHz – 6 GHz frequency was determined through impedance spectroscopy. Real and complex parts of impedance were calculated using the relation given below.

$$Z' = Zcos(\theta) \quad (17)$$

$$Z'' = Zsin(\theta) \quad (18)$$

Z represents the observed modulus of impedance and 'θ' denotes the phase angle. The dielectric factors are connected to the real Z' and imaginary Z'' parts of the impedance as:

$$Z' = \frac{\varepsilon''}{\omega C_{\circ}\left(\varepsilon'^{2}+\varepsilon''^{2}\right)} \quad (19)$$

$$Z'' = \frac{\varepsilon''}{\omega C_o(\varepsilon'^2 + \varepsilon''^2)} \quad (20)$$

Where Z', Z" were complex impedance's resistive and reactive parts [58]. The real part Z' of complex impedance spectra of synthesized Y-type of $Sr_2Ni_2Ga_xFe_{12-x}O_{22}$ ($0.0 \leq x \leq 0.8$ and $\Delta x = 0.2$) samples were shown in Fig. 18. The real part of impedance value was decreased with frequency and merged each other with the increase in frequency. Space charge polarization is the cause of this behavior in polycrystalline ferrite ceramics. The substitution effect of Ga^{3+} Z' will match the applied field frequency in the low-frequency range, but above 6 GHz, it will do so regardless of frequency or substitution level [59, 60].

Figure 19 depicts the variation of the imaginary portion of the impedance (Z") as a function of the applied frequency. The imaginary part of impedance exhibits the decreasing behavior with frequency in the start, and the values of Z" merge other and are independent of frequency in the high-frequency region. The Z" shows the same behavior as Z' with applied frequency.

Fig. 20 shows the Cole-Cole plots of synthesized Y-type of $Sr_2Ni_2Ga_xFe_{12-x}O_{22}$ ($0.0 \leq x \leq 0.8$ and $\Delta x = 0.2$) samples at moderate (room) temperature. Cole-Cole plots were also drawn in connection to other factors, which are shown below [61]:

$$\tan(\delta) = {\varepsilon''}/{\varepsilon'} = {Z'}/{Z''} = {Y'}/{Y''} = {M''}/{M'} \quad (21)$$

The cole-Cole plot describes conducting layers of grains and resistive thin grain boundaries impact on understanding dielectric properties of ferrite materials [62]. In the Cole-Cole plot, we observe two semicircle types that identify the contribution of less resistive grains and high resistive grain boundaries. In the present investigation, all the samples show a single semicircle. High dielectric constant values are evidenced by the high resistance of these materials, which is caused by the influence of grain boundaries [20, 59, 63].

3.5 Surface morphological analysis

SEM analysis was employed to investigate the surface morphology of the Ga^{3+} substituted Y-type ferrite samples with composition $Sr_2Ni_2Ga_xFe_{12-x}O_{22}$ (x=0.00, 0.2, 0.4, 0.6, and 0.8) sintered at 1150 ˚C. In the present finding, the hexagonal plate-like shape of grains is confirmed, as depicted in Fig. 21. This type of shape is desired for microwave-absorbing devices. The SEM

images of all the compositions exposed that close-packed hexagonal shapes were observed with irregular grain size. With increasing the substitution content of Ga, the grain size increases. However, the accumulations of particles were observed due to the chemical changes at high sintering temperatures. The magnetic forces and weak Van der Waals bonds hold these agglomerations. The average grain size was measured in the 0.57-0.89 μm [64, 65].

3.6 Magnetic Properties

The MH loops for all $Sr_2Ni_2Ga_xFe_{12-x}O_{22}$ (x=0.00, 0.2, 0.4, 0.6, and 0.8) Y-type hexagonal ferrites are depicted in Fig. 22 show that all the compositions display a sharp rise in magnetization at the low applied field and slow change at a high applied magnetic field. The variation in magnetic parameters including (M_r), (H_c), (M_s), and squareness ratio (M_r/M_s) with the substitution content of Ga^{3+} were determined from M-H loops are listed in Table 5. The variations in these magnetic parameters are well understood by their cationic stoichiometry and occupancy of these metallic cations in S and T blocks of the ferroxplana Y-type hexagonal ferrite lattice. The y-type hexaferrite crystal structure consists of six different non-equivalent crystallographic sites out of these two tetrahedral ($6c_{IV}$ and $6c_{IV}$) and four octahedral ($3a_{VI}$, $3b_{VI}$, $6c_{VI}$, and $18h_{VI}$) sites are responsible for the magnetic properties of ferrite ceramic materials are depicted in Table 6 [66].

The change in the values of magnetic parameters such as M_s, $H_{c,}$ and M_r with the substitution of Ga^{3+} cations in Sr-Ni Y-type ferrites is shown in Fig. 23. It is clear that both the values of M_s. and M_r. Increase from 68.20 to 71.78 (emu/g) and 31.63 to 33.33 (emu/g) with the increase in substitution content of Ga. The present finding obtained the highest saturation magnetization and retentivity values than the already published results for Y-type hexaferrites. The superexchange interaction in the spinel 'S' block of Y ferrite between tetrahedral $6c_{IV}$ and octahedral $3a_{VI}$ lattice sites of metal cations is responsible for the change in magnetic parameters. The entire magnetization produced in ferrite ceramic samples is determined by the total magnetization of B-sites (octahedral) and A-sites (tetrahedral) sites and the difference between the magnetization of B and A sites [67]. In the present finding, the enhancement in M_s and M_r is due to the distribution of cations among octahedral and tetrahedral crystal structure sites. The replacement of Fe^{3+} ions by the poorly magnetic Ga^{3+} ions in the spin-down magnetic moments of tetrahedral ($6c_{IV}$) and octahedral ($6c_{VI}$) sites. This increase in saturation magnetization and retentivity is due

to the remaining net upward magnetic momentum of Fe^{3+} ions [68, 69]. The decline in coercivity value from 655.86 to 513.64 Oe was observed with the substitution of Ga^{3+}. This decrease in coercivity is directly linked with a reduction in magnetocrystalline anisotropy. In addition, the decline in coercivity is due to the decrease in the porosity of the samples. The coercivity is inversely proportional to saturation magnetization, and many other researchers observed the same behavior.

The Bohr magneton or magnetic moment of $Sr_2Ni_2Ga_xFe_{12-x}O_{22}$ (x=0.00, 0.2, 0.4, 0.6, and 0.8) Y ferrites were calculated by using the relation given below [70]:

$$\text{Magnetic moment} = \frac{M.W \times M_S}{5585}$$

M.W and M_s represent the molecular weight and saturation magnetization of each composition. The values of magnetic momentum increase from 16.05 to 16.97, following the same behavior as that of saturation magnetization [71].

For the single-domain or multi-domain nature of synthesized materials, it is essential to determine their squareness ratio (M_r/M_s). If the squareness ratio is less than 0.5, synthesized materials are multi-domains; otherwise, single domains are natural. In our experimental data, the values of M_r/M_s vary from 0.48 to 0.43, which confirms that the Ga-substituted Y ferrites exhibit a multi-domain nature [72, 73].

Acknowledgement

This research was funded by the Princess Nourah bint Abdulrahman University Researchers Supporting Project number (PNURSP2023R29), Princess Nourah bint Abdulrahman University, Riyadh, Saudi Arabia. The authors extend their appreciation to the Deanship of Scientific Research at King Khalid University for funding this work through Large Groups Project under grant number (RGP.2/228/44).

4. Conclusion

Single phase nanostructure Ga^{3+} substituted ferroxplana ferrite ceramic sample $Sr_2Ni_2Ga_xFe_{12-x}O_{22}$ ($0.00 \leq x \leq 0.8$ and $\Delta x = 0.2$) were manufactured by sol-gel auto ignition synthesis. The specimens were annealed at a comparatively low Temperature of 1150 ˚C for 5.5 hours. Lattice parameters (a, c) vary with the incorporation of Ga^{3+} in the crystal lattice. The crystallite size (D) was measured in the 34 – 41 nm range. FTIR analysis exhibits two characteristic peaks in 444-513 cm^{-1}, confirming metal-oxygen bonds resulting in polycrystalline Y-type hexaferrites. Room Temperature DC resistivity increases (3.78×10^{10}-1.13×10^{11} Ω cm) with the substitution of Ga^{3+} due to its strong preference for octahedral lattice sites. There is a direct relation between resistivity and activation energy. Conduction in the ferromagnetic region below the Curie point is caused by electrons, while polarons are responsible in the paramagnetic region. Multi domains nature of synthesized materials is confirmed by its squareness ratio (0.48-0.43). Coercivity (655.86-507.86 Oe) confirms synthesized materials' soft magnetic nature, which is desirable for longitudinal recording media. Optimized dielectric parameters were achieved with the substitution of Ga^{3+} ions. The high value of resistivity and Q values suggested that these materials are powerful candidates for (MLCIs) components and high-frequency applications.

1. Valenzuela, R., *Novel applications of ferrites.* Physics Research International, 2012. **2012**.
2. Verma, A., et al., *High-resistivity nickel–zinc ferrites by the citrate precursor method.* Journal of magnetism and magnetic materials, 1999. **192**(2): p. 271-276.
3. Rezlescu, N., et al., *MgCu nanocrystalline ceramic with La3+ and Y3+ ionic substitutions used as humidity sensor.* J. Optoelectron. Adv. Mater, 2004. **6**: p. 695.
4. Jeong, K.-P., et al., *Study on Magnetic Properties of the U-Type Ferrite According to Substituted Elements.* Archives of Metallurgy and Materials, 2019. **64**(2).
5. Haijun, Z., et al., *Complex permittivity and permeability dependence of Ba4Zn2− ZCoZFe36O60 U-type hexaferrites prepared by citrate sol–gel on composition, annealing temperature and frequency.* Materials Science and Engineering: B, 2003. **97**(2): p. 160-166.
6. Jeong, K.-P., et al., *Microwave absorption characteristics of U-type ferrite powders according to substitution elements and its compositions.* Metals and Materials International, 2021. **27**(8): p. 2782-2790.
7. Kashid, P., et al., *Influence of Co++ ion concentration on magnetic and microwave properties of Ba (4− X) Co (2+ X) Fe36O60 (Ba-MY) hexaferrite.* Journal of Materials Science: Materials in Electronics, 2018. **29**(3): p. 1748-1758.
8. Ahmad, M., et al., *Temperature dependent structural and magnetic behavior of Y-type hexagonal ferrites synthesized by sol–gel autocombustion.* Journal of Alloys and Compounds, 2015. **651**: p. 749-755.
9. Smit, J., *Ferrites.* Philips Technical Laboratory, 1959: p. 278-280.

10. Khan, M.A., et al., *Effects of Dy on structural, dielectric and magnetic properties of Ni-Sr-Y co-precipitated hexaferrites.* Ceramics International, 2018. **44**(18): p. 22255-22261.
11. Mahmood, S.H., et al. *Modification of the magnetic properties of Co2Y hexaferrites by divalent and trivalent metal substitutions*. in *Solid State Phenomena*. 2016. Trans Tech Publ.
12. Malik, H., et al., *Structural, spectral, thermal and dielectric properties of Nd-Ni co-doped Sr-Ba-Cu hexagonal ferrites synthesized via sol-gel auto-combustion route.* Ceramics International, 2018. **44**(1): p. 605-612.
13. Pullar, R.C., *Hexagonal ferrites: A review of the synthesis, properties and applications of hexaferrite ceramics.* Progress in Materials Science, 2012. **57**(7): p. 1191-1334.
14. Ahmad, M., et al., *Effects of Sr-substitution on the structural and magnetic behavior of Ba-based Y-type hexagonal ferrites.* Journal of Alloys and Compounds, 2013. **580**: p. 23-28.
15. Murtaza, G., et al., *Structural and magnetic properties of Nd–Mn substituted Y-type hexaferrites synthesized by microemulsion method.* Journal of Alloys and Compounds, 2014. **602**: p. 122-129.
16. Aen, F., M. Ahmad, and M.U. Rana, *The role of Ga substitution on magnetic and electromagnetic properties of nano-sized W-type hexagonal ferrites.* Current Applied Physics, 2013. **13**(1): p. 41-46.
17. Rehman, A.u., et al., *Synthesis and investigations of structural, magnetic and dielectric properties of Cr-substituted W-type Hexaferrites for high frequency applications.* Journal of Electroceramics, 2021. **46**(3): p. 93-106.
18. Akhtar, M.N., et al., *Structural elucidation and magnetic behaviour evaluation of gallium substituted garnet ferrites.* Ceramics International, 2018. **44**(18): p. 22504-22511.
19. Mahmood, M.A., et al., *impact of cadmium substitution on the structural, spectral, dielectric and magnetic properties of Z-type hexaferrites synthesized via sol-gel route.* Ceramics International, 2021. **47**(17): p. 24852-24859.
20. Majeed, A., et al., *Influence of Cr and Zn substitution on structural, magnetic and dielectric properties of Sr2-xZnxNi2Fe28-yCryO46 X-type hexagonal ferrite.* Solid State Sciences, 2020. **100**: p. 106090.
21. Yu, X., et al., *Effect of Zn2+-Sn4+ co-substitution on structural and magnetic properties of SrFe12-2xZnxSnxO19 (x = 0–2) M-type strontium ferrite.* Physica B: Condensed Matter, 2023. **653**: p. 414676.
22. Gui, D. and X. Ren, *Investigation on electromagnetic properties of La–Al co-doped Co2W hexagonal ferrites for microwave absorption.* Ceramics International, 2023.
23. ur Raheem, F., et al., *Structural, spectral, electrical, dielectric and magnetic properties of Yb doped SrNiCo-X hexagonal nano-structured ferrites.* Journal of Alloys and Compounds, 2017. **708**: p. 903-910.
24. Azhar Khan, M., et al., *Structural spectral, dielectric, and magnetic properties of Mg substituted Ba3CoFe24O41 Z-type hexaferrites.* Journal of Magnetism and Magnetic Materials, 2022. **560**: p. 169589.
25. Jotania, R.B. and H.S. Virk. *Y-type Hexaferrites: structural, dielectric and magnetic properties*. in *Solid State Phenomena*. 2012. Trans Tech Publ.
26. Warhate, V.V., V.D. Badwaik, and D.S. Badwaik, *AC Conductivity and Dielectric Properties of TiCo Substituted Y-type Strontium Nano Hexa-ferrites Prepared by Sol Gel Auto-combustion.* Materials Today: Proceedings, 2019. **15**: p. 490-497.
27. Mohammed, J., et al., *Crystal structure refinement and the magnetic and electro-optical properties of Er3+–Mn2+-substituted Y-type barium hexaferrites.* Ceramics International, 2021. **47**(13): p. 18455-18465.
28. Asif, R.M., et al., *synthesis and characterization of Tb doped Ni–Zn nano ferrites as substrate material for dual band MIMO antenna.* Physica B: Condensed Matter, 2023. **653**: p. 414658.

29. Chandel, M., et al., *A review on structural, electrical and magnetic properties of Y-type hexaferrites synthesized by different techniques for antenna applications and microwave absorbing characteristic materials.* AIMS Materials Science, 2020. **7**(3): p. 244-268.
30. Idrees, M., et al., *Structural and dielectric properties of Sr4Zn2Fe36O60 U-type hexaferrites with optimized Gd contents and sintered by a two-step process.* Ceramics International, 2022.
31. Gulbadan, S., et al., *investigation of crystal structure, photoluminescence, and Raman studies of Sm–Co substituted Ba–Sr M-type hexaferrites.* Ceramics International, 2023.
32. Tahir, W., et al., *Comprehensive study of structural, physical, and spectroscopic properties of Co-Ni substituted BaMg2Fe16O27 W-type hexaferrites.* Journal of Taibah University for Science, 2021. **15**(1): p. 1196-1209.
33. Salunkhe, M.Y., D.S. Choudhary, and D.K. Kulkarni, *Infrared absorption studies of the system Sr2Me2Fe12O22.* Vibrational Spectroscopy, 2004. **34**(2): p. 221-224.
34. Adeela, N., et al., *Structural and magnetic response of Mn substituted Co2 Y-type barium hexaferrites.* Journal of Alloys and Compounds, 2016. **686**: p. 1017-1024.
35. Carol T, T.T., et al., *Crystal-structure analysis, Raman spectroscopy, dielectric measurements, magnetic and optical properties of Cr3+–Ni2+-substituted Co2Y-type barium hexaferrites.* Materials Research Bulletin, 2022. **145**: p. 111564.
36. Mukhtar, G., et al., *investigation of crystal structure, dielectric response and magnetic properties of Tb3+ substituted Co2 Y-type barium hexaferrites.* Solid State Sciences, 2021. **113**: p. 106549.
37. Irfan, M., et al., *Effect of Y2O3 doping on the electrical transport properties of Sr2MnNiFe12O22 Y-type hexaferrite.* Current Applied Physics, 2014. **14**(1): p. 112-117.
38. Iqbal, M.J., *Synthesis and study of physical properties of Zr4+–Co2+ co-doped barium hexagonal ferrites.* Materials Science and Engineering: B, 2009. **164**(1): p. 6-11.
39. Iqbal, M.J. and F. Liaqat, *Physical and Electrical Properties of Nanosized Mn- and Cr-Doped Strontium Y-Type Hexagonal Ferrites.* Journal of the American Ceramic Society, 2010. **93**(2): p. 474-480.
40. Arshad, M.I., et al., *Structural, optical, electrical, dielectric, molecular vibrational and magnetic properties of La3+ doped Mg–Cd–Cu ferrites prepared by Co-precipitation technique.* Ceramics International, 2022. **48**(10): p. 14246-14260.
41. Ahmad, B., et al., *Synthesis, dielectric and magnetic properties of Mn-Ge substituted Co2Y hexaferrites.* Journal of Saudi Chemical Society, 2019. **23**(4): p. 407-416.
42. Ahmad, B., et al., *Magnetic and dielectric properties of Nd–Mn substituted Co2Y-hexaferrites.* Journal of Magnetism and Magnetic Materials, 2018. **460**: p. 171-176.
43. Ali, I., et al., *Effect of Eu–Ni substitution on electrical and dielectric properties of Co–Sr–Y-type hexagonal ferrite.* Materials Research Bulletin, 2014. **49**: p. 338-344.
44. Ahmad, B., et al., *synthesis and electrical behavior of Ni-Ti substituted Y-type hexaferrites for high frequency application.* Journal of Magnetism and Magnetic Materials, 2018. **451**: p. 787-792.
45. Elahi, A., et al., *Preparation and properties of sol–gel synthesized Mg-substituted Ni2Y hexagonal ferrites.* Ceramics International, 2013. **39**(2): p. 983-990.
46. Kamran, M. and M. Anis-ur-Rehman, *Influence of La3+ substitutions on structural, dielectric and electrical properties of spinel cobalt ferrite.* Ceramics International, 2023. **49**(4): p. 7017-7029.
47. Manzoor, A., et al., *Effect of Ho3+ ions on microwave losses and high-temperature electrical behavior of Li-based magnetic oxides.* Ceramics International, 2021. **47**(4): p. 4633-4642.
48. Ali, I., et al., *study of electrical and dielectric behavior of Tb+3 substituted Y-type hexagonal ferrite.* Journal of Alloys and Compounds, 2014. **617**: p. 863-868.

49. Hussain, K., N. Amin, and M.I. Arshad, *Evaluation of structural, optical, dielectric, electrical, and magnetic properties of Ce3+ doped Cu0.5Cd0.25Co0.25Fe2-xO4 spinel nano-ferrites.* Ceramics International, 2021. **47**(3): p. 3401-3410.
50. Amin, N., et al., *Structural, electrical, optical and dielectric properties of yttrium substituted cadmium ferrites prepared by Co-Precipitation method.* Ceramics International, 2020. **46**(13): p. 20798-20809.
51. Ali, I., et al., *Role of grain boundaries in the conduction of Eu–Ni substituted Y-type hexaferrites.* Journal of Magnetism and Magnetic Materials, 2014. **362**: p. 115-121.
52. Ahmad, B., et al., *Elucidation of structure and conduction mechanism in Nd-Mn substituted Y-type strontium hexaferrites.* Journal of Alloys and Compounds, 2017. **723**: p. 9-16.
53. Wu, J., et al., *Sm-doped enhanced magnetic-dielectric properties of low-temperature fired Co2Z ferrite materials for high-frequency device applications.* Ceramics International, 2023. **49**(5): p. 8502-8507.
54. Junaid, M., et al., *Impact of Bi–Cr substitution on the structural, spectral, dielectric and magnetic properties of Y-type hexaferrites.* Ceramics International, 2020. **46**(16, Part A): p. 25478-25484.
55. Kamran, M. and M. Anis-ur-Rehman, *Study of dielectric and electrical properties in Co-(Fe–Ce-Nd) nanosized spinel ferrites.* Materials Science in Semiconductor Processing, 2023. **153**: p. 107111.
56. Lodhi, M.Y., et al., *Unveiling the effect of Gd–Co co-substitution in the enrichment of structural and dielectric properties of SrBaMn based magnetic oxide.* Ceramics International, 2022. **48**(6): p. 8612-8619.
57. Kausar, R., et al., *investigation into the structural and magnetic features of nickel doped U-type hexaferrites prepared through sol–gel method.* Journal of Magnetism and Magnetic Materials, 2022. **549**: p. 169054.
58. Odeh, I., et al., *Dielectric and magnetic properties of Zn-substituted Co2Y barium hexaferrite prepared by sol–gel auto combustion method.* Physica B: Condensed Matter, 2016. **494**: p. 33-40.
59. Costa, M.M., G.F.M. Pires Júnior, and A.S.B. Sombra, *Dielectric and impedance properties' studies of the of lead doped (PbO)-Co2Y type hexaferrite (Ba2Co2Fe12O22 (Co2Y)).* Materials Chemistry and Physics, 2010. **123**(1): p. 35-39.
60. Behera, P. and S. Ravi, *Magnetic and dielectric spectroscopic studies in Zn substituted Y-type barium hexaferrite.* Journal of Alloys and Compounds, 2018. **767**: p. 712-723.
61. Arshad, M., et al., *Investigation of crystal structure, electrical and dielectric response of Zr4+ - Co2+ substituted Ba–Sr–Ni Y-type hexagonal ferrites synthesized by sol-gel route.* Ceramics International, 2022.
62. Sahu, B.B., et al., *Electrical properties of Y-type hexaferrite.* Journal of Advanced Dielectrics, 2018. **8**(03): p. 1850022.
63. Ali, I., et al., *Effect of Tb–Mn substitution on DC and AC conductivity of Y-type hexagonal ferrite.* Journal of Alloys and Compounds, 2013. **579**: p. 576-582.
64. Ali, I., et al., *Role of Tb–Mn substitution on the magnetic properties of Y-type hexaferrites.* Journal of Alloys and Compounds, 2014. **599**: p. 131-138.
65. Rehman, A.U., et al., *Controllable synthesis of La3+ doped Zn0.5Co0.25Cu0.25Fe2−xLaxO4 (x = 0.0, 0.0125, 0.025, 0.0375, 0.05) nano-ferrites by sol-gel auto-combustion route.* Ceramics International, 2020. **46**(18, Part A): p. 29297-29308.
66. Ali, I., et al., *Synthesis and magnetic properties of (Eu–Ni) substituted Y-type hexaferrite by surfactant assisted co-precipitation method.* Journal of Magnetism and Magnetic Materials, 2015. **385**: p. 386-393.

67. Dhruv, P.N., et al., *Design and development of Ga-substituted Z-type hexaferrites for microwave absorber applications: Mössbauer, static and dynamic properties.* Ceramics International, 2021. **47**(1): p. 1145-1162.
68. Iqbal, M.J., M.N. Ashiq, and P.H. Gomez, *Effect of doping of Zr–Zn binary mixtures on structural, electrical and magnetic properties of Sr-hexaferrite nanoparticles.* Journal of alloys and compounds, 2009. **478**(1-2): p. 736-740.
69. Khan, M.A., et al., *Structural, spectral, dielectric and magnetic properties of Sr2CuxNi2-xFe28-xCrxO46 (0 ≤ x ≥ 0.5) ferrites synthesized via micro-emulsion route.* Materials Chemistry and Physics, 2021. **259**: p. 124066.
70. Lodhi, M.Y., et al., *Structural, magnetic and dielectric properties of Dy-Co substituted Sr-Ba-Mg-based magnetic oxides.* Applied Physics A, 2021. **127**: p. 1-15.
71. Suthar, M., et al., *Structural, magnetic, and biocompatibility evaluations of chromium substituted barium hexaferrite (Co2–Y) for hyperthermia application.* Materials Chemistry and Physics, 2023. **296**: p. 127348.
72. Mohammed, I., et al., *Effect of Dy3+-Cu2+ doping on structural, magnetic and electromagnetic properties of Co2Y-type hexaferrite.* Ceramics International, 2023.
73. Majeed, A., et al., *Tuning the Properties of Novel Magnetic Oxide via Co–Bi Co-substitution Including Theoretical Background of Characterization Techniques.* Journal of Superconductivity and Novel Magnetism, 2021. **34**(9): p. 2313-2329.

Table 1

Various structural parameters including lattice parameters ('a' and 'c'), volume of unit cell (V_{cell}), full width at half maxima (β), crystallite size (D), bulk density (D_b), x-ray density (D_x) and porosity P (%), specific surface area (S) and Microstrain (ε) of $Sr_2Ni_2Ga_xFe_{12-x}O_{22}$ ($0.00 \leq x \leq 0.8$ and $\Delta x = 0.2$).

X	0.00	0.2	0.4	0.6	0.8
d (Å)	2.51	2.5	2.5	2.51	2.51
β (˚)	0.2202	0.2411	0.2301	0.1997	0.218
D (nm)	37.48	34.25	35.88	41.33	37.86
a (Å)	5.89	5.78	5.80	5.89	5.89
c (Å)	43.54	43.38	43.48	43.60	43.57
c/a	7.39	7.49	7.39	7.40	7.39
V(Å^3)	1307.42	1257.93	1302.19	1308.87	1310.61
D_x (g.cm^{-3})	5.01	5.22	5.05	5.04	5.04
D_b (g.cm^{-3})	3.21	3.28	3.36	3.22	3.39
P (%)	35.86	37.15	33.47	35.94	32.74
Molecular weight (amu)	1314.76	1317.54	1320.31	1323.09	1325.86
S (10^7cm^{2}g^{-1})	31.95	33.56	33.11	28.8	31.44
Dislocation density δ (10^{-3} nm^{-2})	0.71	0.85	0.78	0.58	0.7
Microstrain ε (10^{-3})	2.98	3.25	3.11	2.7	2.95
Stacking fault coefficient (α)	0.0004	0.007	0.004	0.0004	0.0004

Table 2

DC electrical resistivity (ρ_{DC}) at 303 K, curie temperature, activation energy of paramagnetic region (Ep), activation energy of ferromagnetic region (E_f) and drift mobility (μ_d) of Gd^{3+} substituted Y-type hexaferrites $Sr_2Ni_2Ga_xFe_{12-x}O_{22}$ ($0.00 \leq x \leq 0.8$ and $\Delta x = 0.2$).

X	ρ at 303 K (Ω cm)	T_c (K)	PM region E_p (eV)	FM region E_f (eV)	$\Delta E=E_p-E_f$ (eV)	μ_d at 303 K ($cm^2v^{-1}s^{-1}$)
0.00	3.78×10^{10}	333	0.57	0.15	0.42	9.46×10^{-15}
0.2	9.51×10^{10}	333	0.54	0.15	0.39	3.71×10^{-15}
0.4	1.92×10^{10}	333	0.55	0.35	0.20	1.82×10^{-14}
0.6	3.89×10^{10}	353	0.63	0.19	0.44	9.57×10^{-15}
0.8	1.13×10^{11}	343	0.64	0.03	0.61	3.19×10^{-15}

Table 3

Comparison of the DC electrical resistivity with different Y-type hexaferrites at 303 K.

Sr.No.	Compound Composition	Synthesis method	ρ_{dc} (Ω cm)	Reference
1	$Sr_2Co_2Ti_{0.5}Ni_{0.5}Fe_{11}O_{22}$	Sol-gel	4.9×10^9	[44]
2	$Sr_2Co_1Ni_{1.0}Eu_{0.1}Fe_{11.90}O_{22}$	Microemulsion	3.07×10^9	[43]
3	$Ba_2Zn_2Tb_{0.10}Fe_{11.90}O_{22}$	Sol-gel	4.73×10^8	[48]
4	$Sr_2Ni_{1.4}Mn_{0.6}Fe_{10.5}Cr_{1.5}O_{22}$	Sol-gel	7.37×10^9	[39]
5	$Sr_{1.90}Nd_{0.01}Co_2Mn_1Fe_{11}O_{22}$	Sol-gel	2.376×10^9	[52]
6	$Sr_2Ni_2Ga_{0.80}Fe_{11.20}O_{22}$	Sol-gel	1.13×10^{11}	Present Work

Table: 4

Comparative study of dielectric constant (ε') and dielectric loss (ε'') for Y-type hexagonal ferrites at different frequency regions 1 MHz, 3 GHz and 6 G Hz with other researcher work.

Sr. No.	Composition	1 MHz		3 GHz		6 GHz		Reference
		ε'	ε''	ε'	ε''	ε'	ε''	
01	$Sr_2Co_2Fe_{12-2x}Mn_xGe_xO_{22}$ (x=0.0, 0.1, 0.2, 0.3, 0.4, 0.5)	14.70 To 11.25	5.80 To 2.90	14.80 To 7.5	2.80 To 0.50	--	--	[41]
02	$Sr_2Co_2Fe_{12-2x}Ti_xNi_xO_{22}$ (x=0.0, 0.1, 0.2, 0.3, 0.4, 0.5)	16.0 To 6.0	2.40 To 1.0	14.10 To 3.10	1.70 To 0.40	--	--	[44]
03	$Sr_2Ni_2Dy_x Fe_{12-x}O_{22}$ (x=0.0, .05, .10, .15, .20, .25)	5.60 To 3.80	0.45 To 0.24	5.50 To 3.60	0.20 To 0.22	--	--	[10]
04	$SrBaCu_{2-x}Ni_xNd_yFe_{12-y}O_{22}$ (x=0-1.0, y=0.0-0.1)	5.10 To 2.50	1.20 To 0.34	3.20 To 2.20	0.45 To 1.0	--	--	[12]
05	$SrBaNi_2Zr_xCo_xFe_{12-2x}O_{22}$ (x=0.0, 0.25, 0.50, 0.75, 1.0)	2.99 To 4.71	0.01 To 0.71	2.27 To 2.68	0.30 To 0.77	2.76 To 3.46	0.65 To 1.41	[61]
06s	$Sr_2Ni_2Ga_xFe_{12-x}O_{22}$ (x=0.00, 0.2, 0.4, 0.6, 0.8)	2.91 To 3.16	0.00 To 0.00	2.21 To 2.30	0.24 To 0.29	2.60 To 2.70	0.34 To 0.44	Present work

Table: 5

Magnetic parameters of $Sr_2Ni_2Ga_xFe_{12-x}O_{22}$ (x=0.00, 0.2, 0.4, 0.6 and 0.8) measured at room temperature.

Sr. No.	Ga^{3+} content (x)	Ms (emu/g)	Mr (emu/g)	Hc (Oe)	Mr/Ms	n_B
1	0.0	68.20	31.63	655.86	0.46	16.05
2	0.2	64.12	30.92	507.86	0.48	15.13
3	0.4	71.78	33.33	619.60	0.46	16.97
4	0.6	69.40	31.23	446.58	0.45	16.44
5	0.8	70.22	30.36	513.64	0.43	16.67

Table: 6

Distribution of the ions and spin orientation for the various sub-lattices of Y-type hexagonal ferrite.

Sublattice	Coordination	Block	Number of ions	Spin
$6c_{IV}$	Tetrahedral	S	2	Down
$3a_{VI}$	Octahedral	S	1	Up
$18h_{VI}$	Octahedral	S-T	6	Up
$6c_{VI}$	Octahedral	T	2	Down
$6c_{IV}$	Tetrahedral	T	2	Down
$3b_{VI}$	Octahedral	T	1	Up

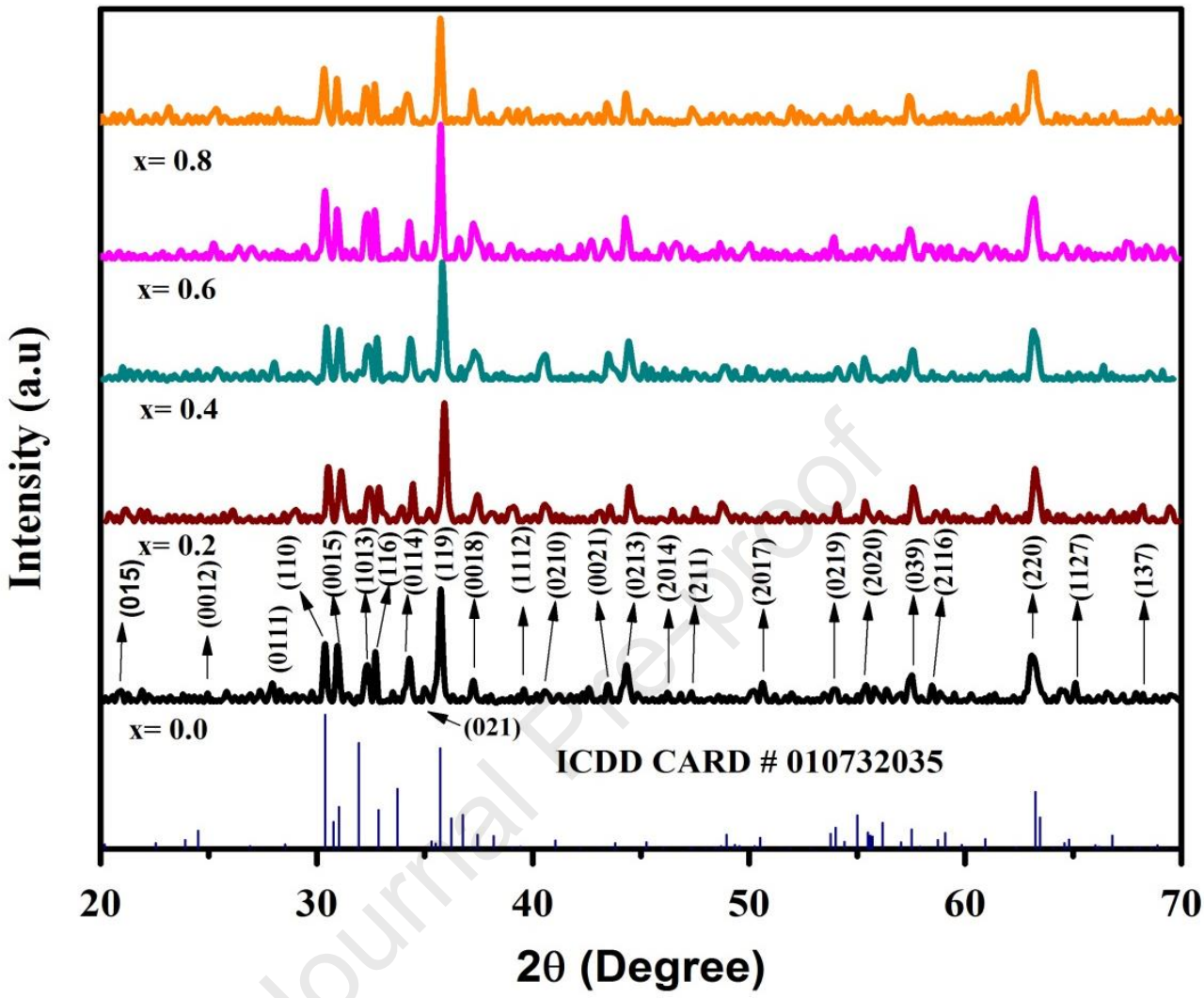

Fig. 1. XRD patterns for $Sr_2Ni_2Ga_xFe_{12-x}O_{22}$ ($0.00 \leq x \leq 0.8$ and $\Delta x = 0.2$) Y-type hexagonal ferrites.

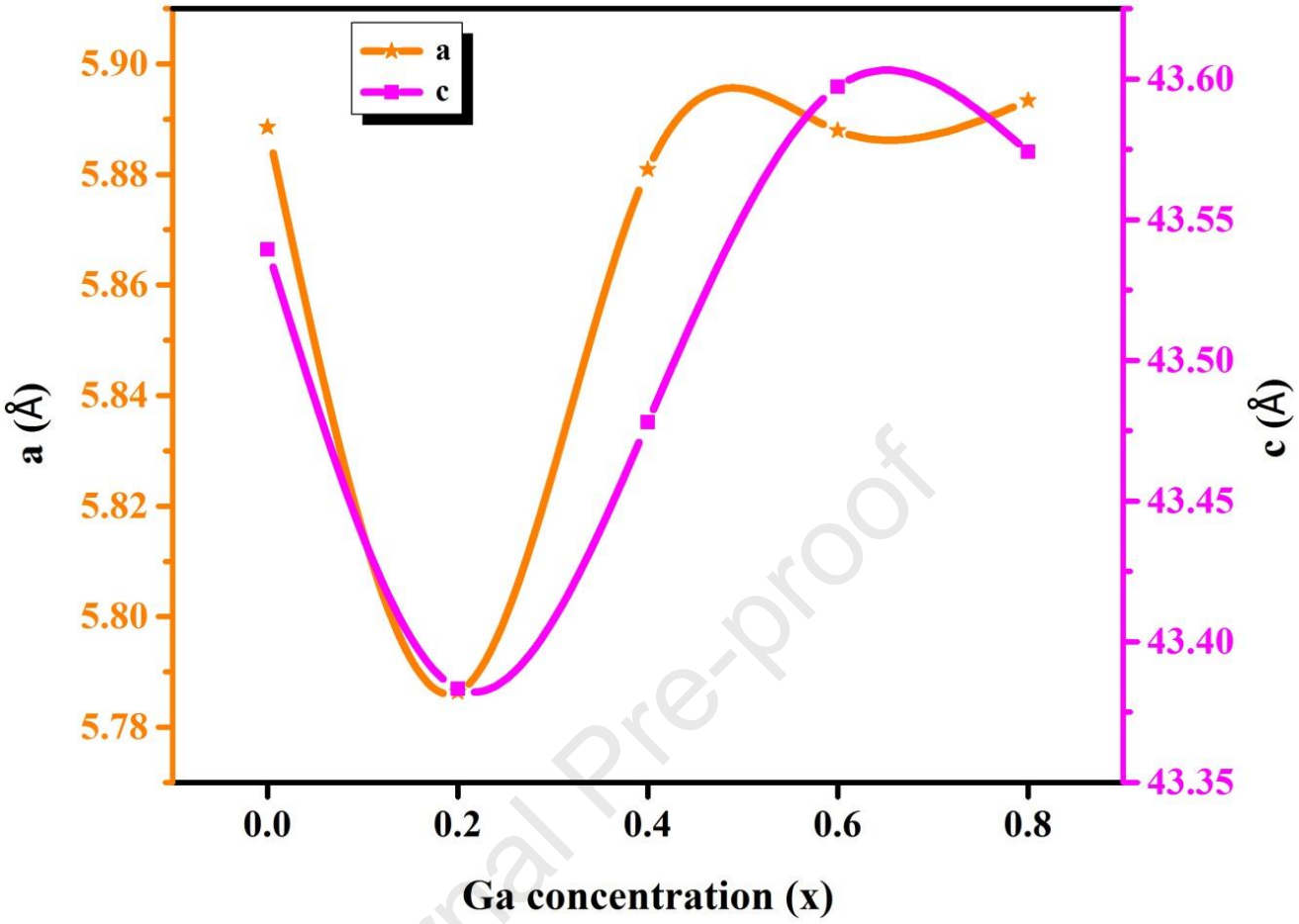

Fig. 2. Variation in lattice parameter "a" and "c" of $Sr_2Ni_2Ga_xFe_{12-x}O_{22}$ ($0.00 \leq x \leq 0.8$ and $\Delta x = 0.2$) hexagonal ferrites.

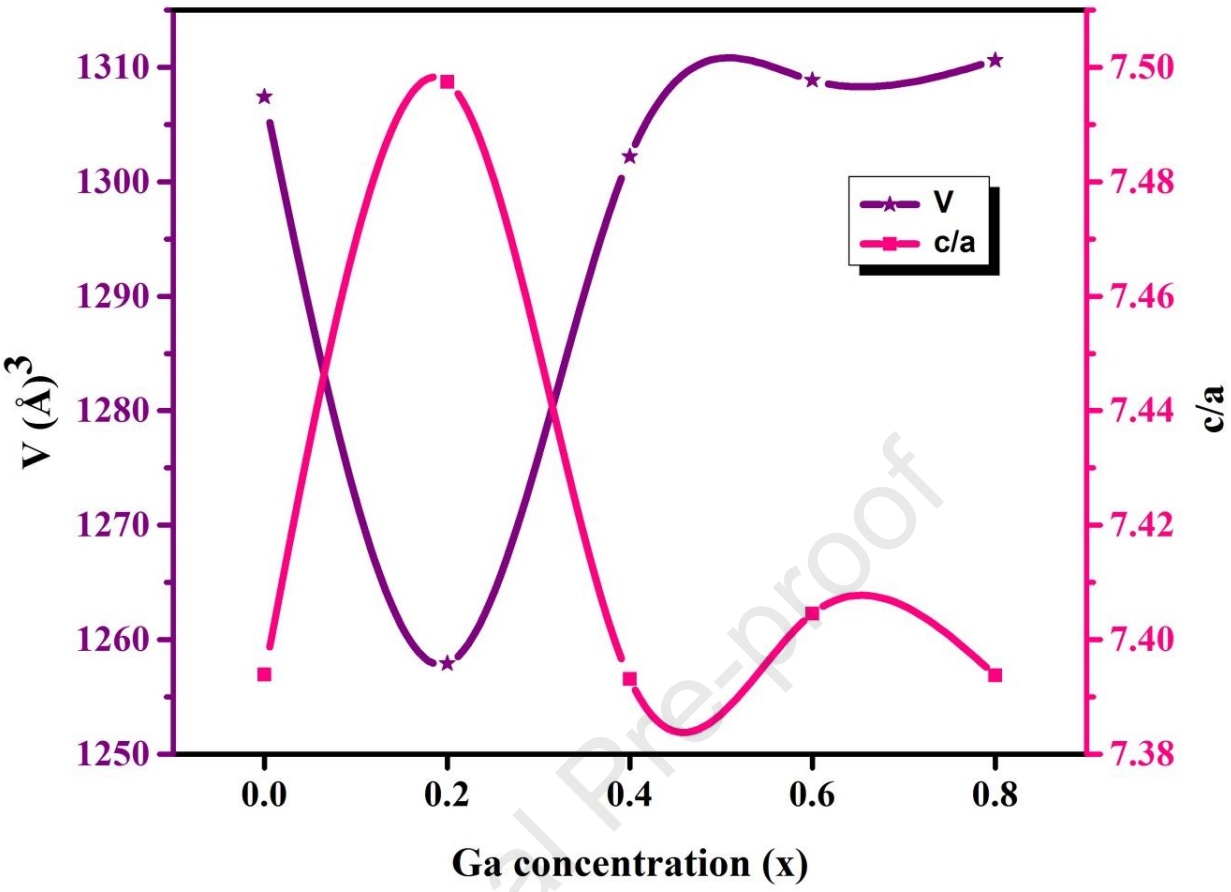

Fig. 3. Variation in unit cell volume and c/a with Ga^{3+} substitution content (x).

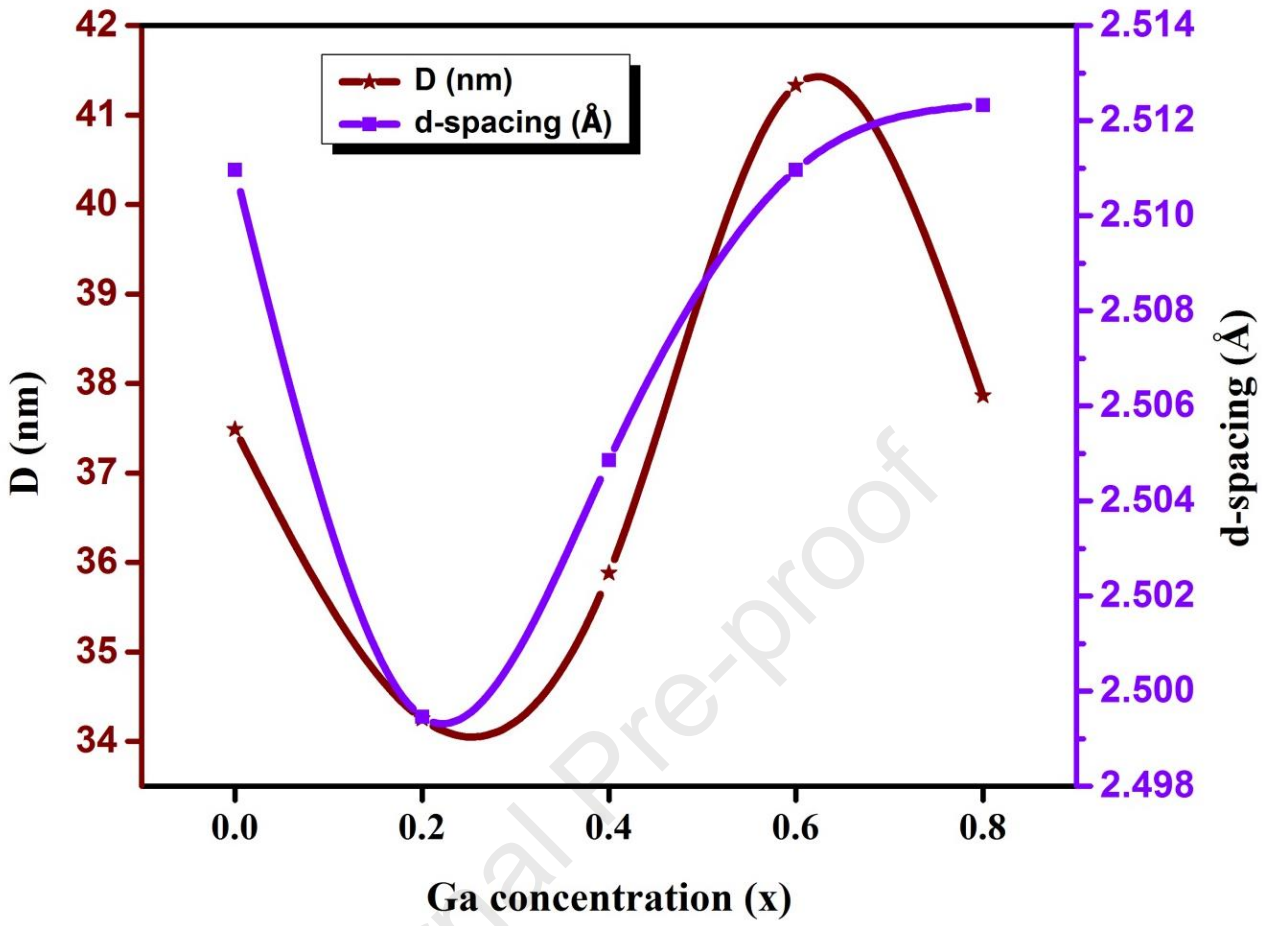

Fig. 4. Variation in crystallite size (D) and d-spacing of $Sr_2Ni_2Ga_xFe_{12-x}O_{22}$ ($0.00 \leq x \leq 0.8$ and $\Delta x = 0.2$) hexagonal ferrites.

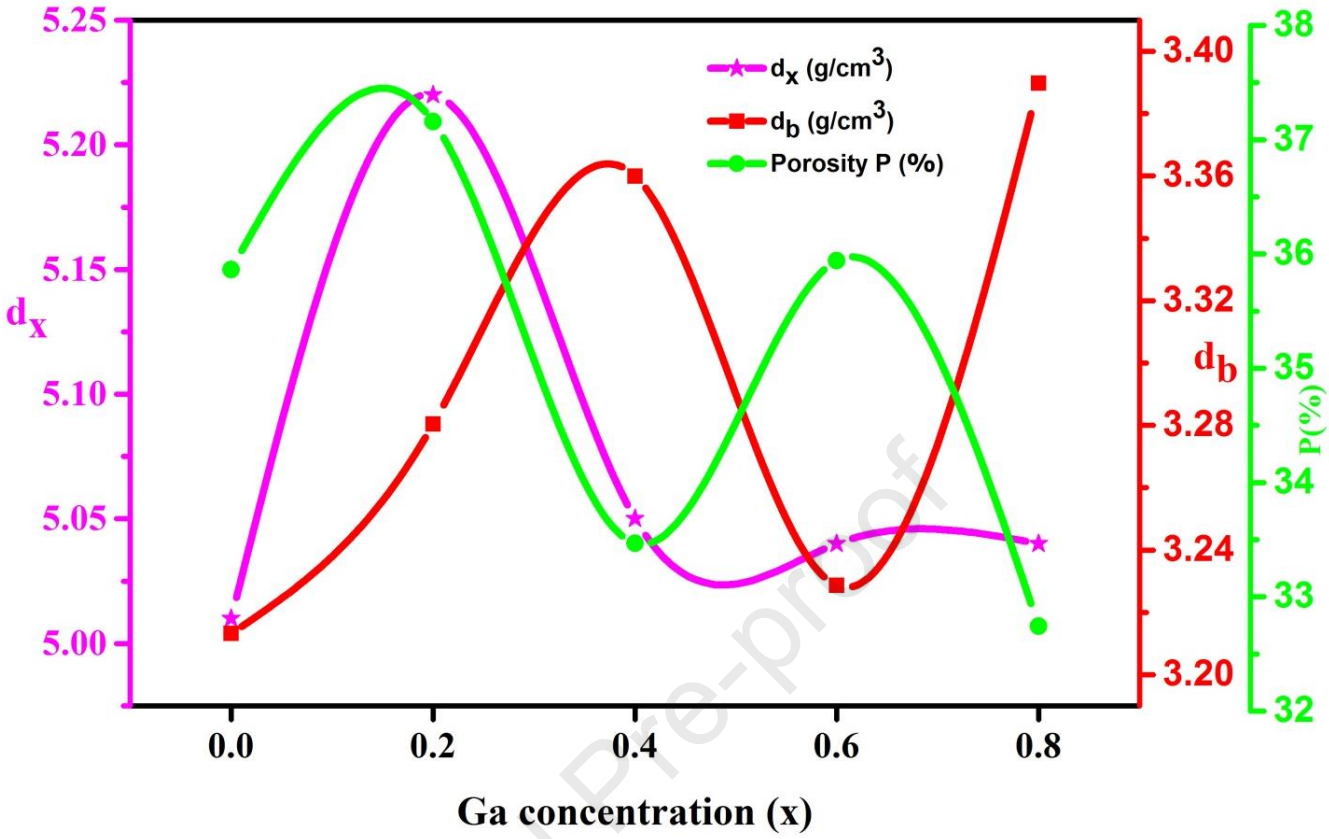

Fig. 5. Variation in X-ray density, experimental density and porosity with substitution content of Ga^{3+}.

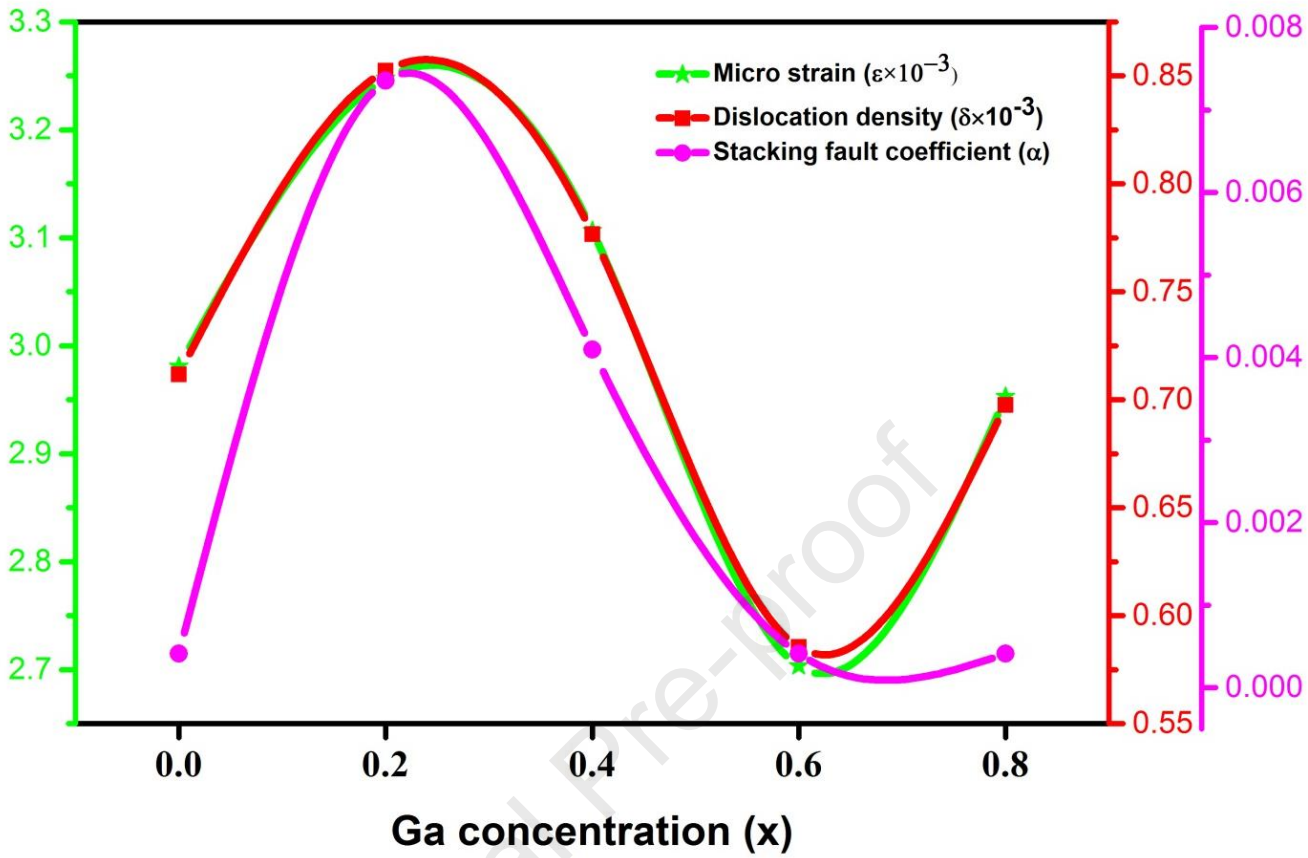

Fig. 6. Variation in Dislocation density (δ), Micro strain (ε), and Stacking fault coefficient (α) with substitution content of Ga.

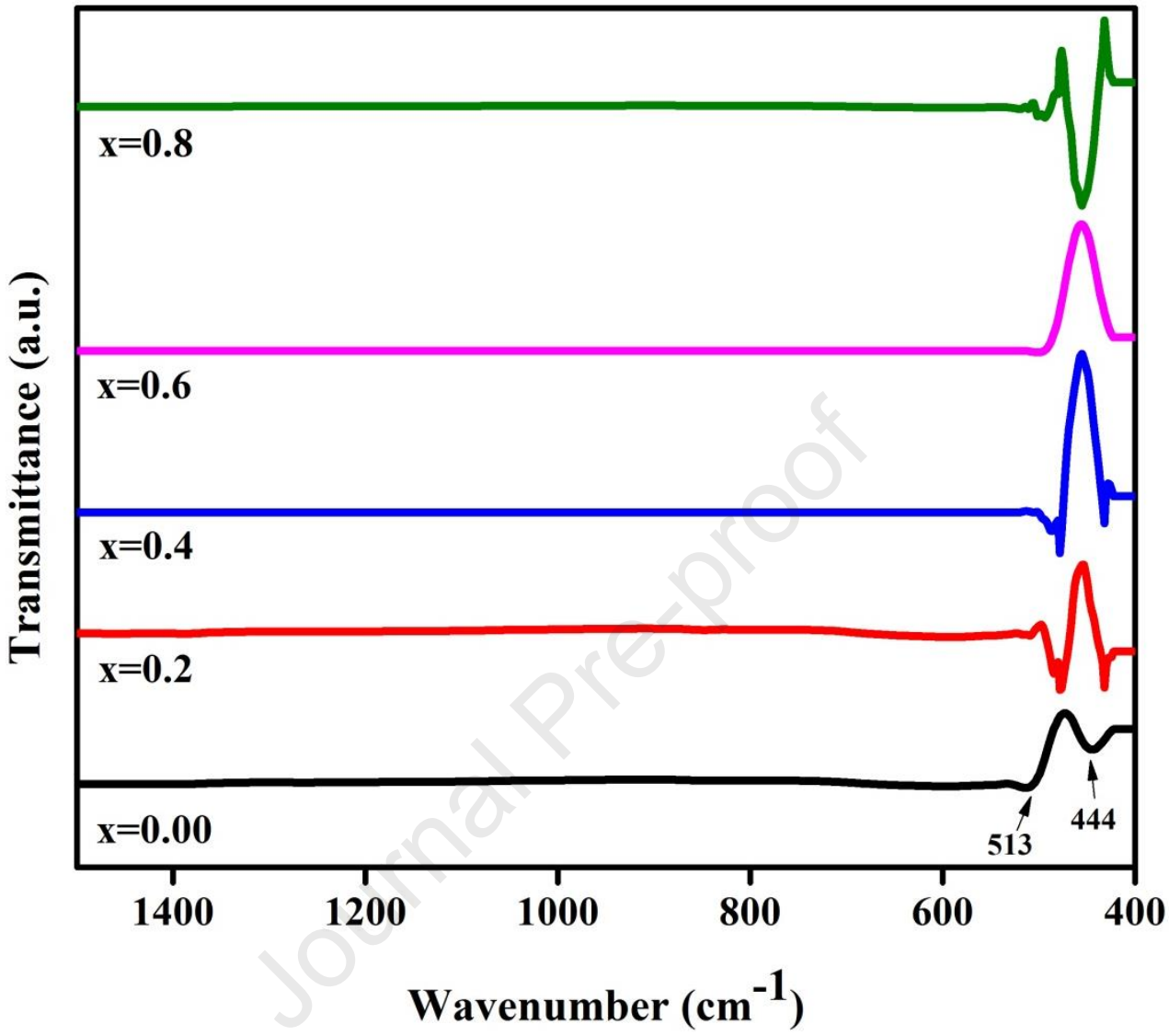

Fig. 7. FTIR spectra of $Sr_2Ni_2Ga_xFe_{12-x}O_{22}$ ($0.0 \leq x \leq 0.8$ and $\Delta x = 0.2$) Y-type hexagonal ferrites.

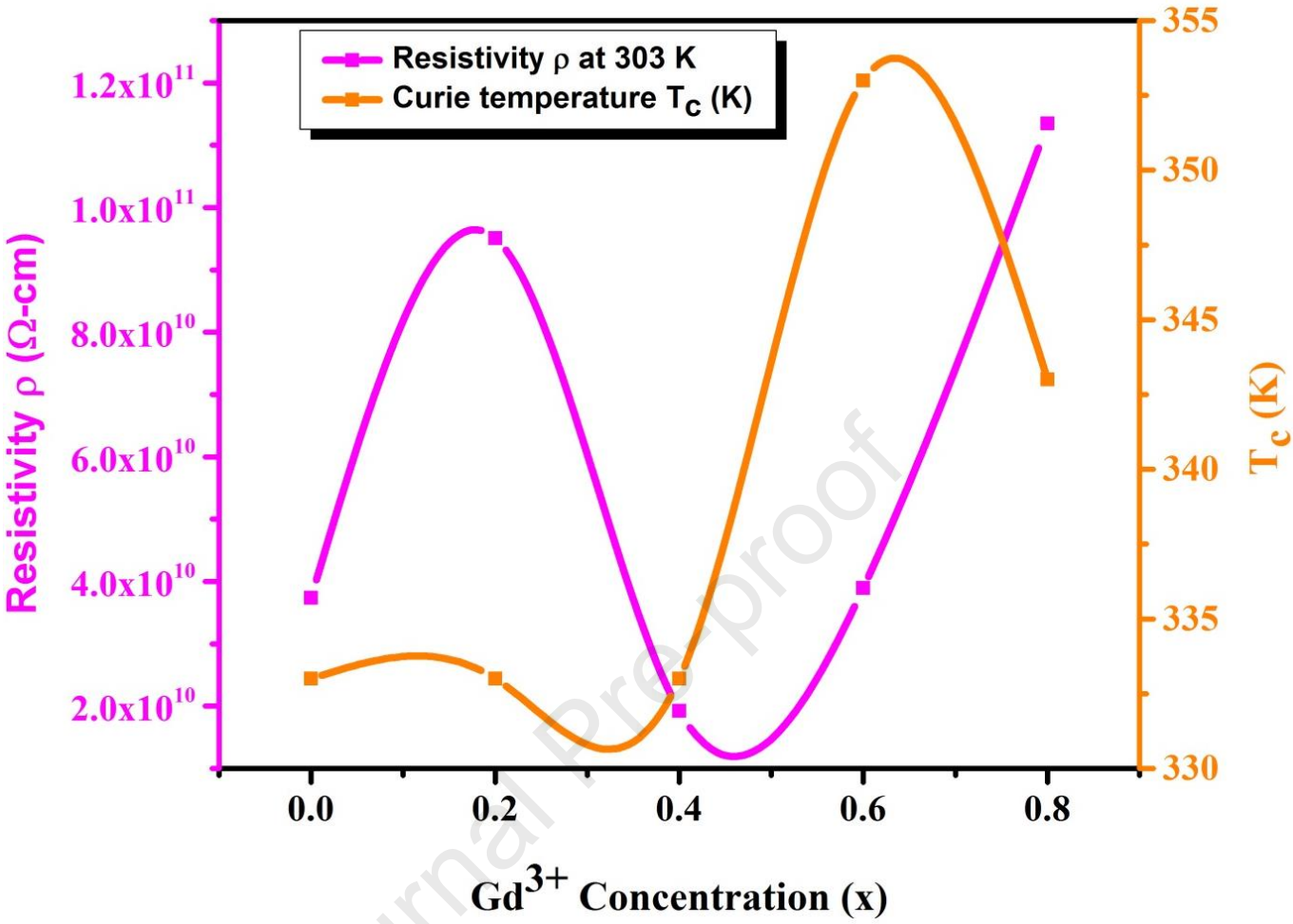

Fig. 8. Variation in DC electrical resistivity (ρ_{dc}) and Curie temperature (T_c) of $Sr_2Ni_2Ga_xFe_{12-x}O_{22}$ ($0.00 \leq x \leq 0.8$ and $\Delta x = 0.2$) Y-type hexagonal ferrites.

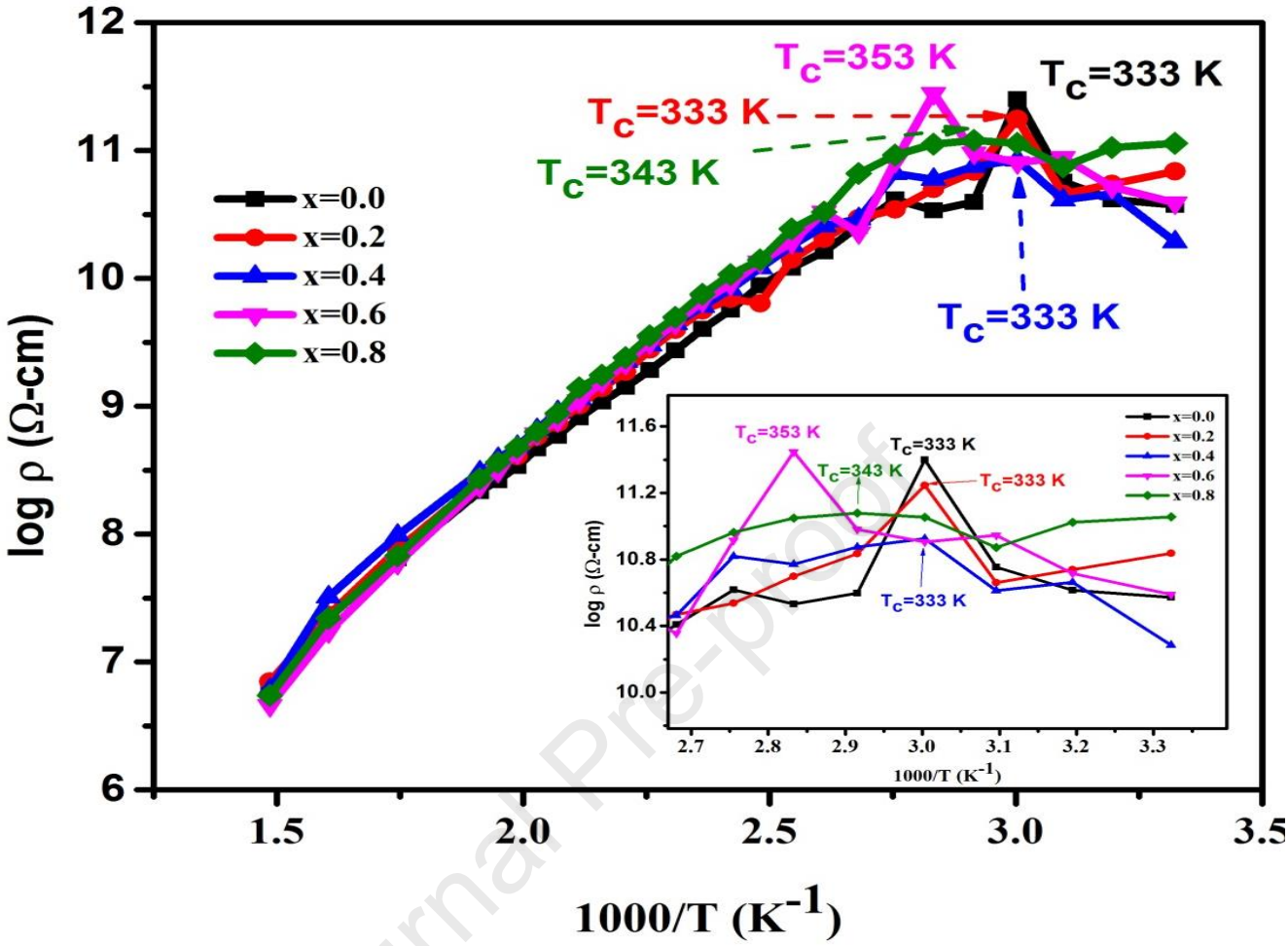

Fig. 9. 1000/T versus log ρ of Ga^{3+} substituted $Sr_2Ni_2Ga_xFe_{12-x}O_{22}$ ($0.00 \leq x \leq 0.8$ and $\Delta x = 0.2$) Y-type hexagonal ferrites. Inset clearly shows the Curie temperature after which the ferrimagnetic materials become paramagnetic materials.

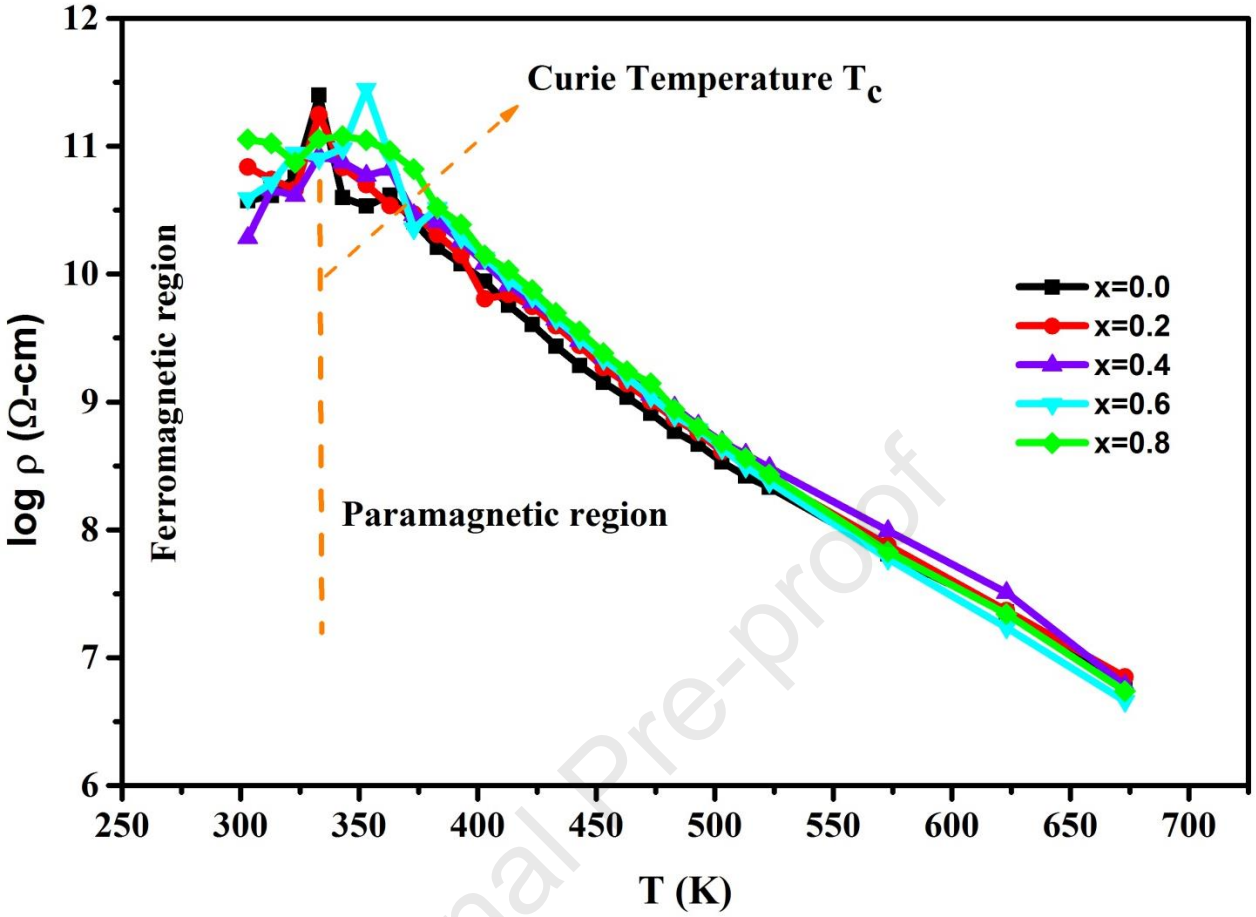

Fig. 10. Temperature T (K) versus log of DC resistivity of Ga^{3+} substituted $Sr_2Ni_2Ga_xFe_{12-x}O_{22}$ ($0.00 \leq x \leq 0.8$ and $\Delta x = 0.2$) Y-type hexagonal ferrites.

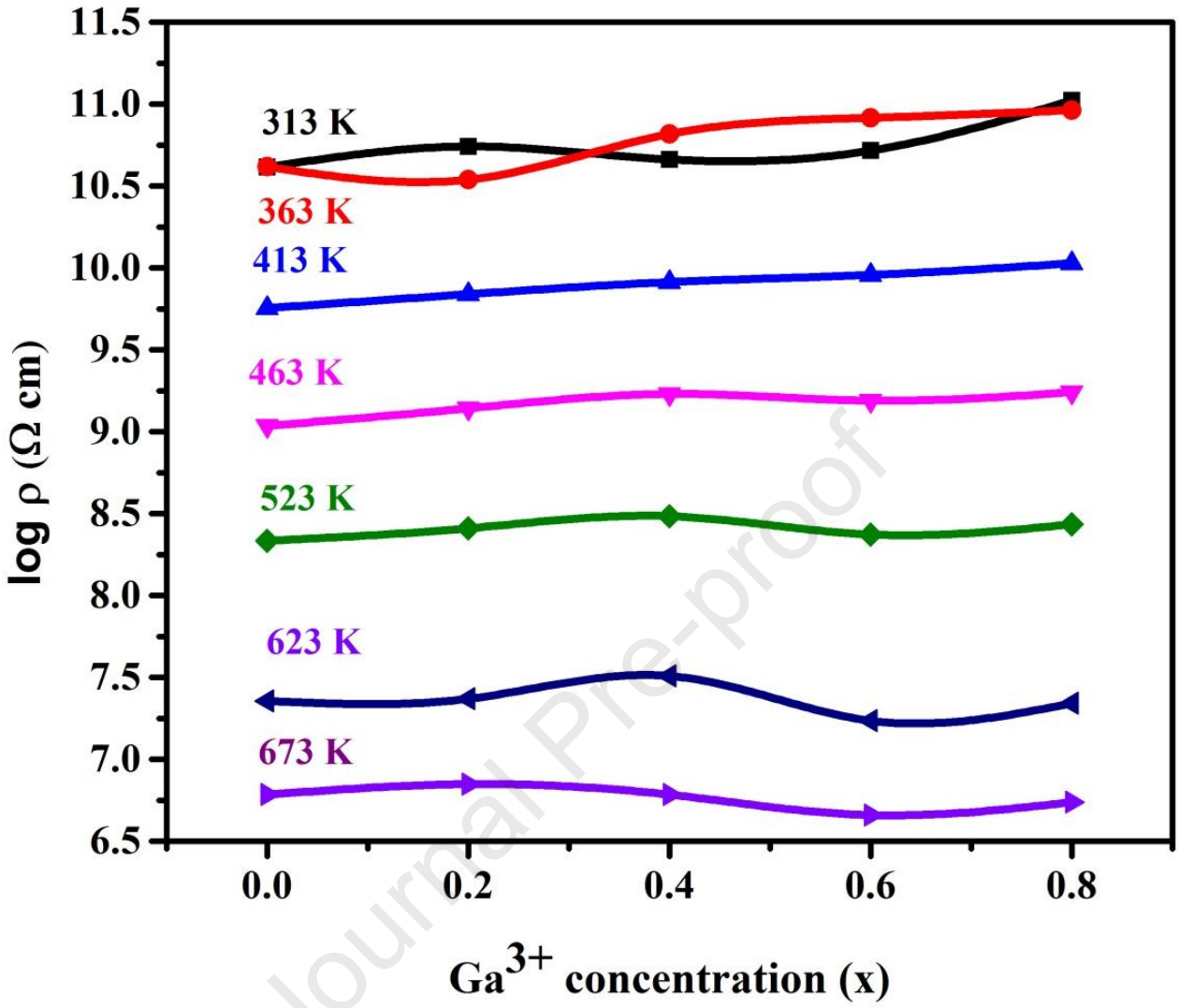

Fig. 11. Graph between log of resistivity and concentration content of Ga^{3+} substituted $Sr_2Ni_2Ga_xFe_{12-x}O_{22}$ ($0.00 \leq x \leq 0.8$ and $\Delta x = 0.2$) Y-type hexagonal ferrites at different temperature range (313 K-673 K).

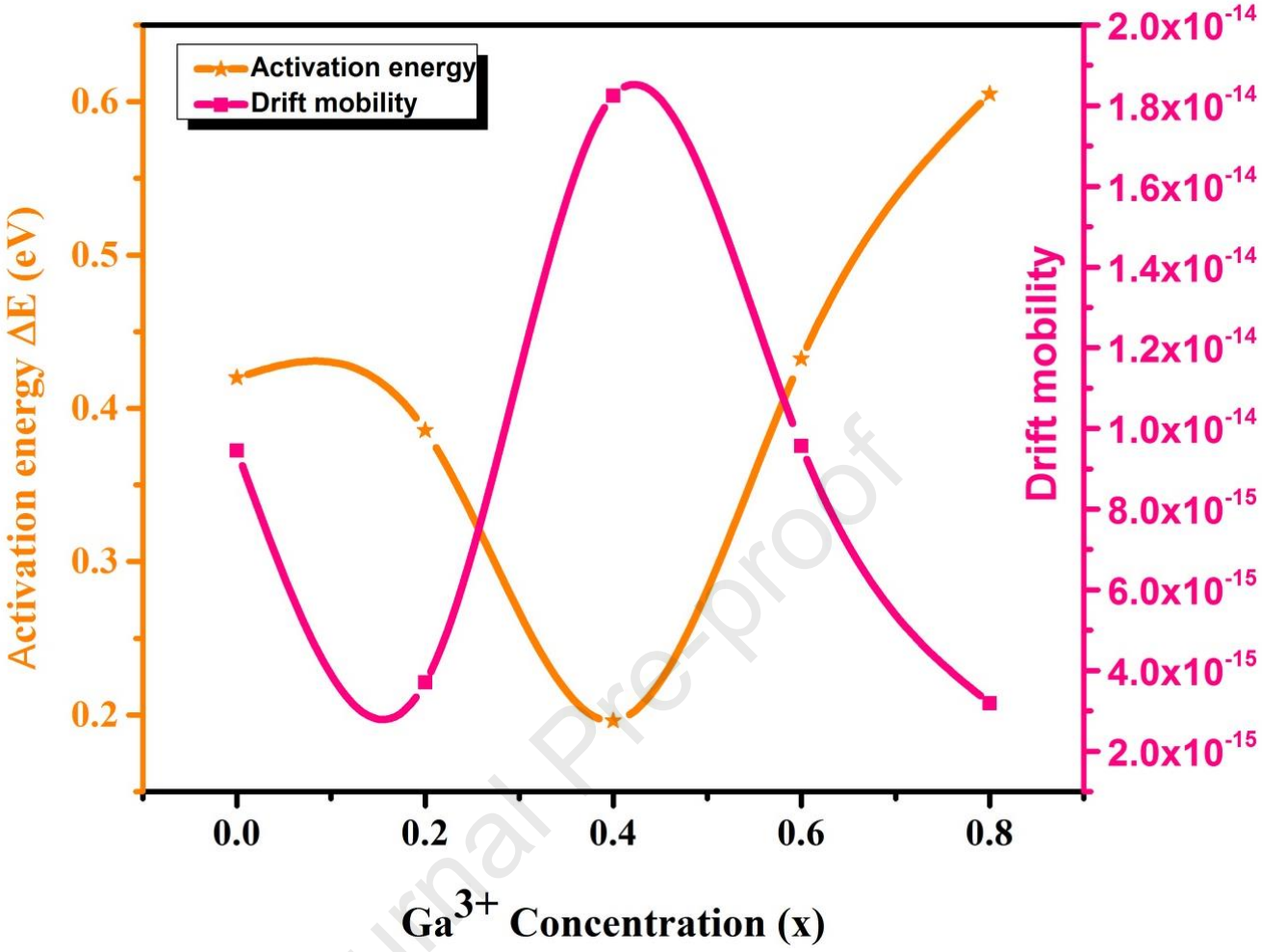

Fig. 12. Graphical representation of activation energy (ΔE) and drift mobility with substitution content of Ga^{3+}.

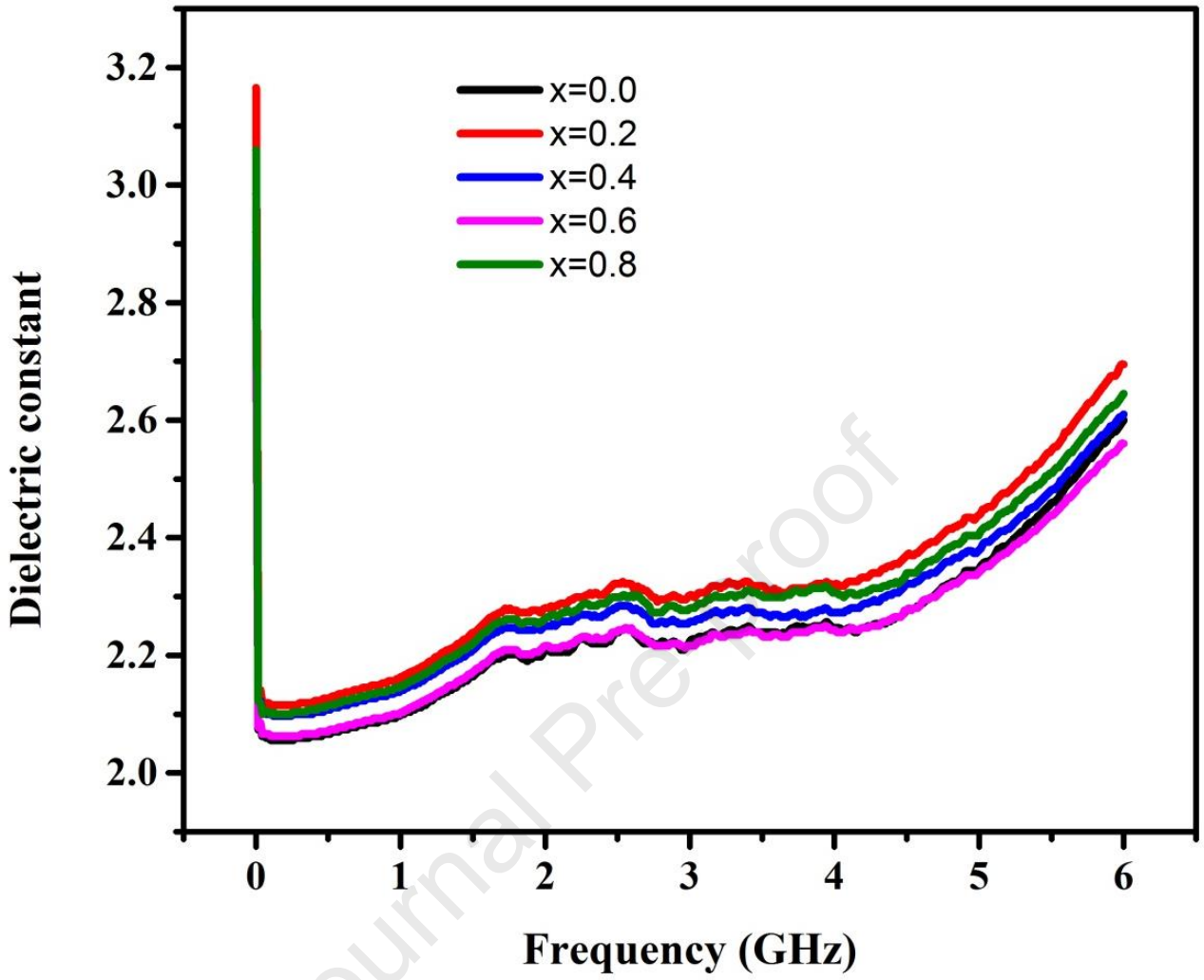

Fig. 13. The variation in dielectric constant values of $Sr_2Ni_2Ga_xFe_{12-x}O_{22}$ ($0.00 \leq x \leq 0.8$ and $\Delta x = 0.2$) Y-type ferrites with applied frequency.

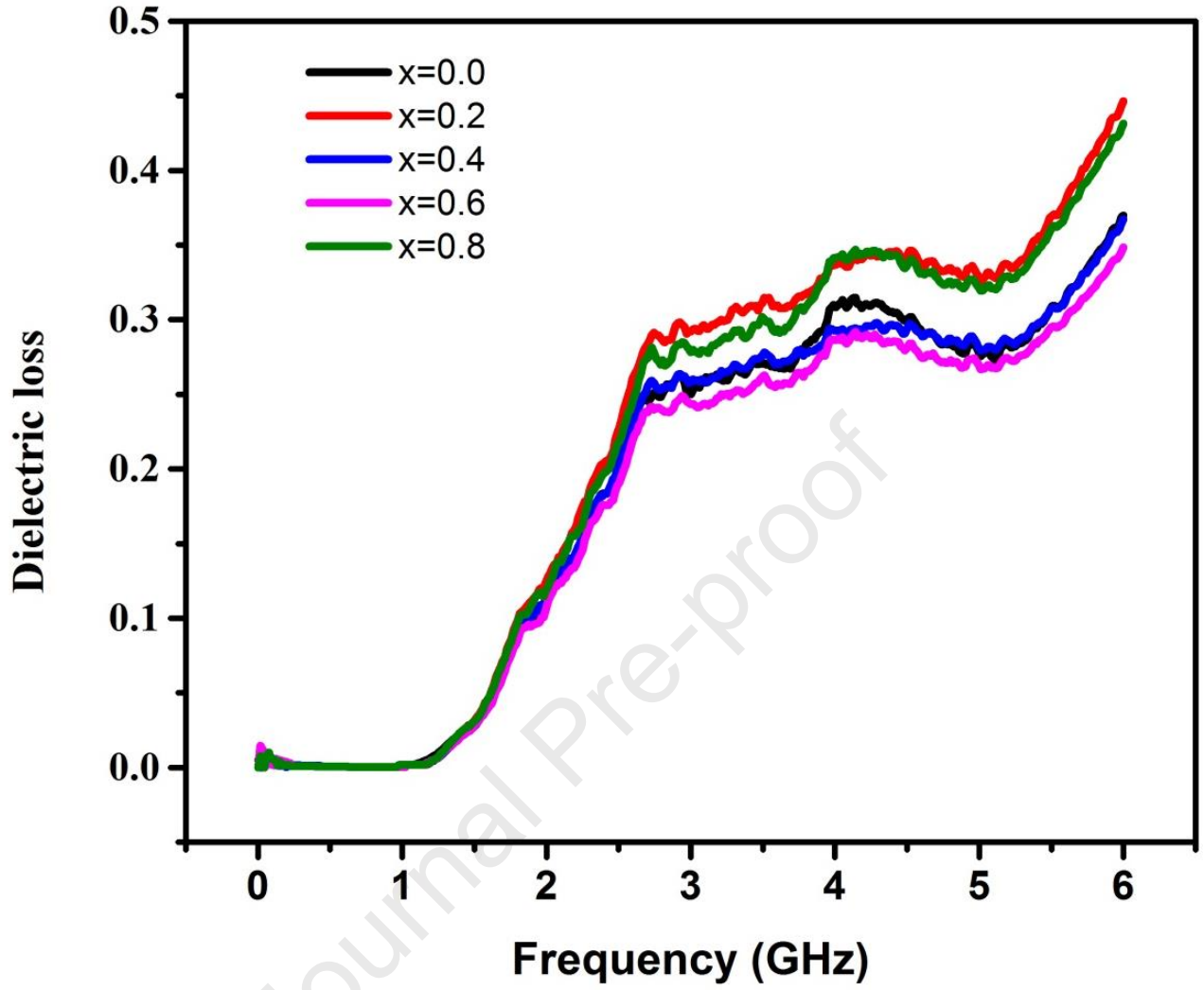

Fig. 14. The variation in dielectric loss values of $Sr_2Ni_2Ga_xFe_{12-x}O_{22}$ ($0.00 \leq x \leq 0.8$ and $\Delta x = 0.2$) Y-type ferrites with applied frequency.

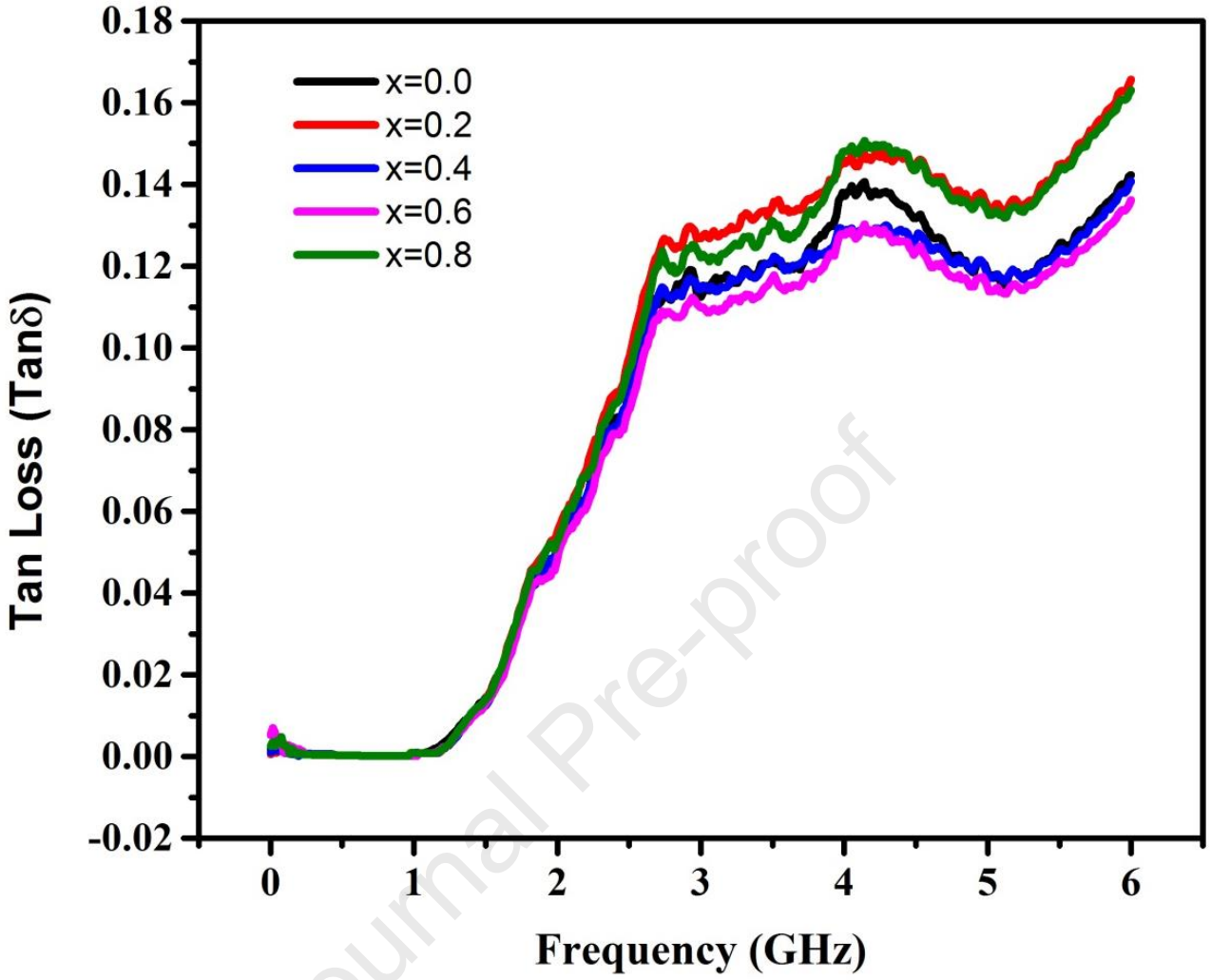

Fig. 15. The variation in Tan loss values of $Sr_2Ni_2Ga_xFe_{12-x}O_{22}$ ($0.00 \leq x \leq 0.8$ and $\Delta x = 0.2$) Y-type ferrites with applied frequency.

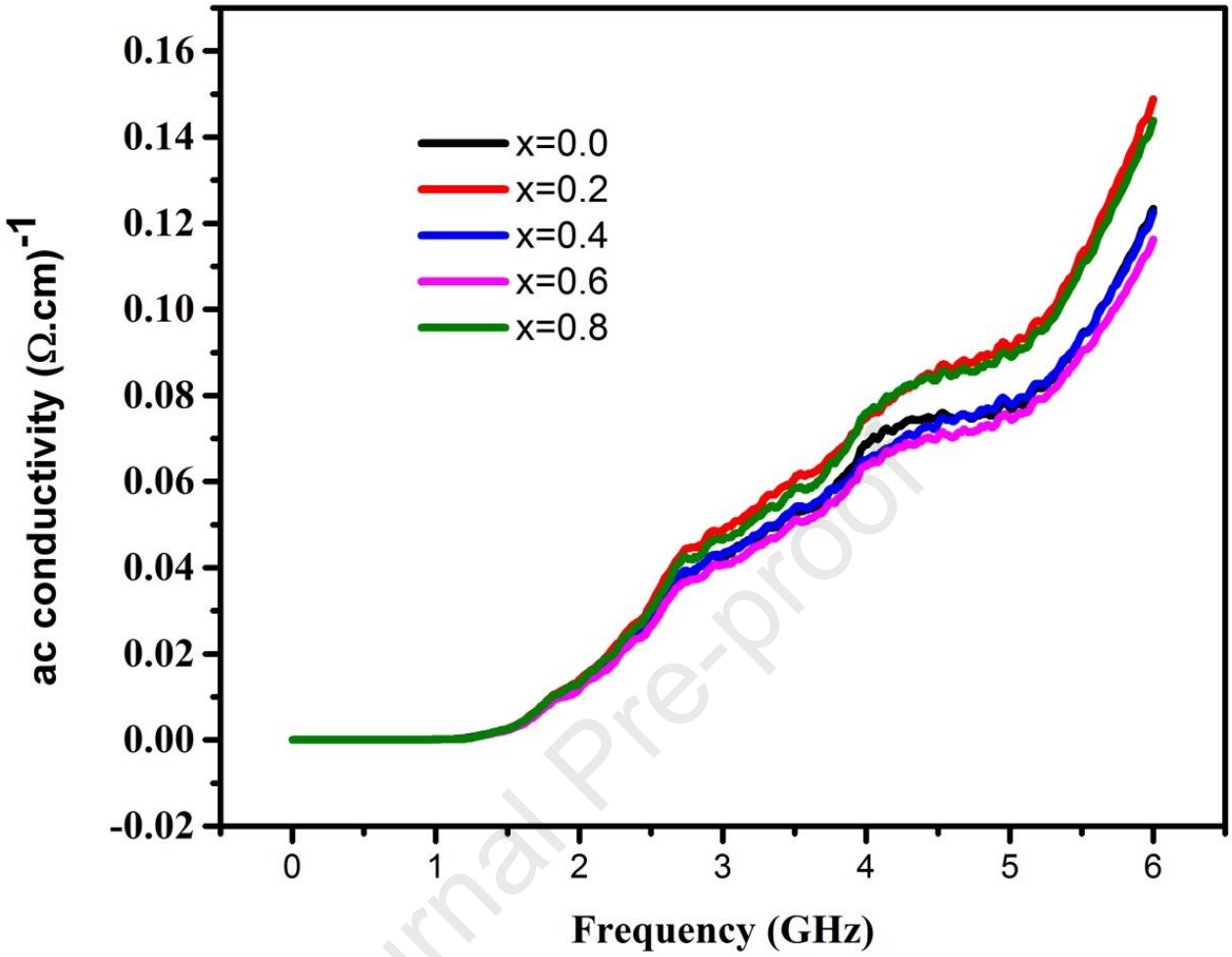

Fig. 16. The variation in ac conductivity values of $Sr_2Ni_2Ga_xFe_{12-x}O_{22}$ ($0.00 \leq x \leq 0.8$ and $\Delta x = 0.2$) Y-type ferrites with applied frequency.

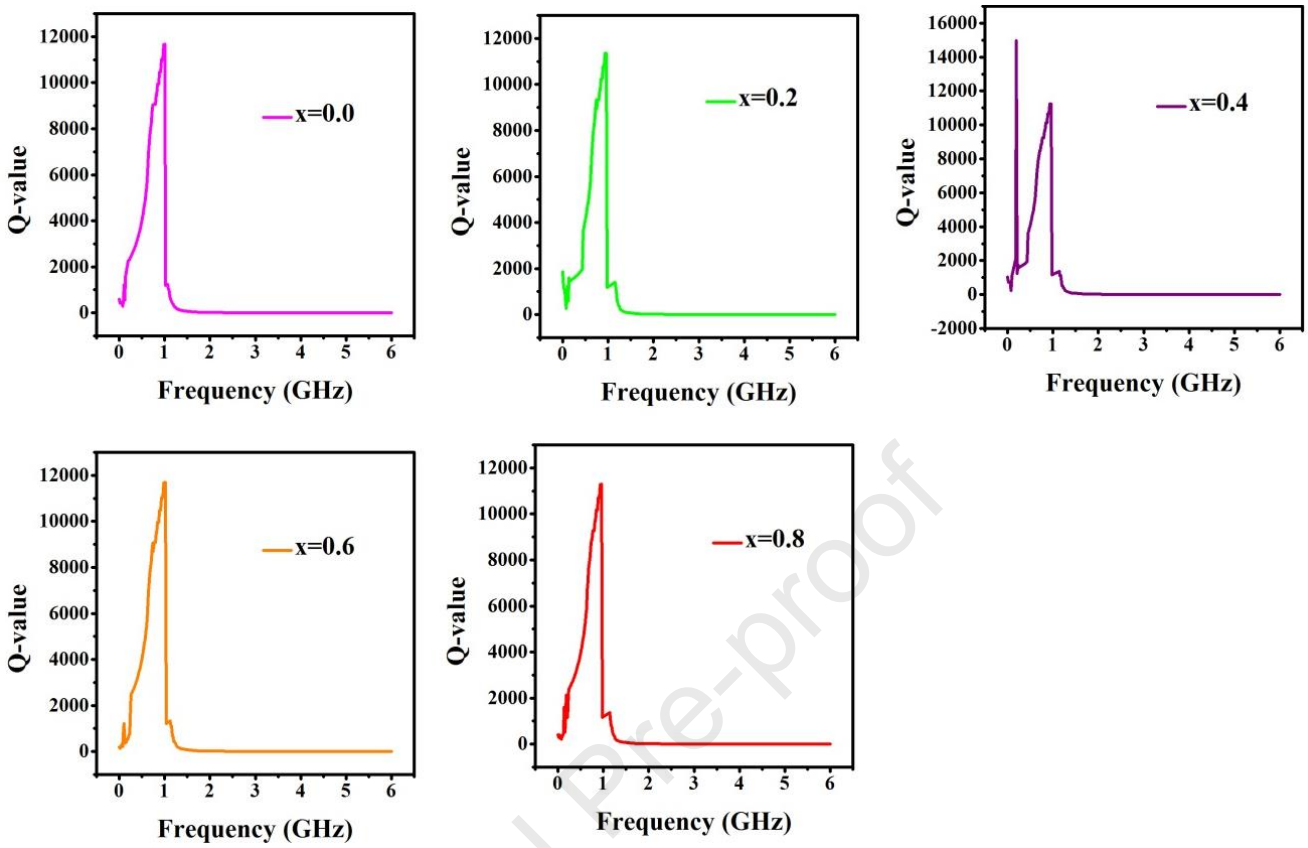

Fig. 17. The variation in Q-values versus frequency of $Sr_2Ni_2Ga_xFe_{12-x}O_{22}$ ($0.00 \leq x \leq 0.8$ and $\Delta x = 0.2$) Y-type hexaferrites.

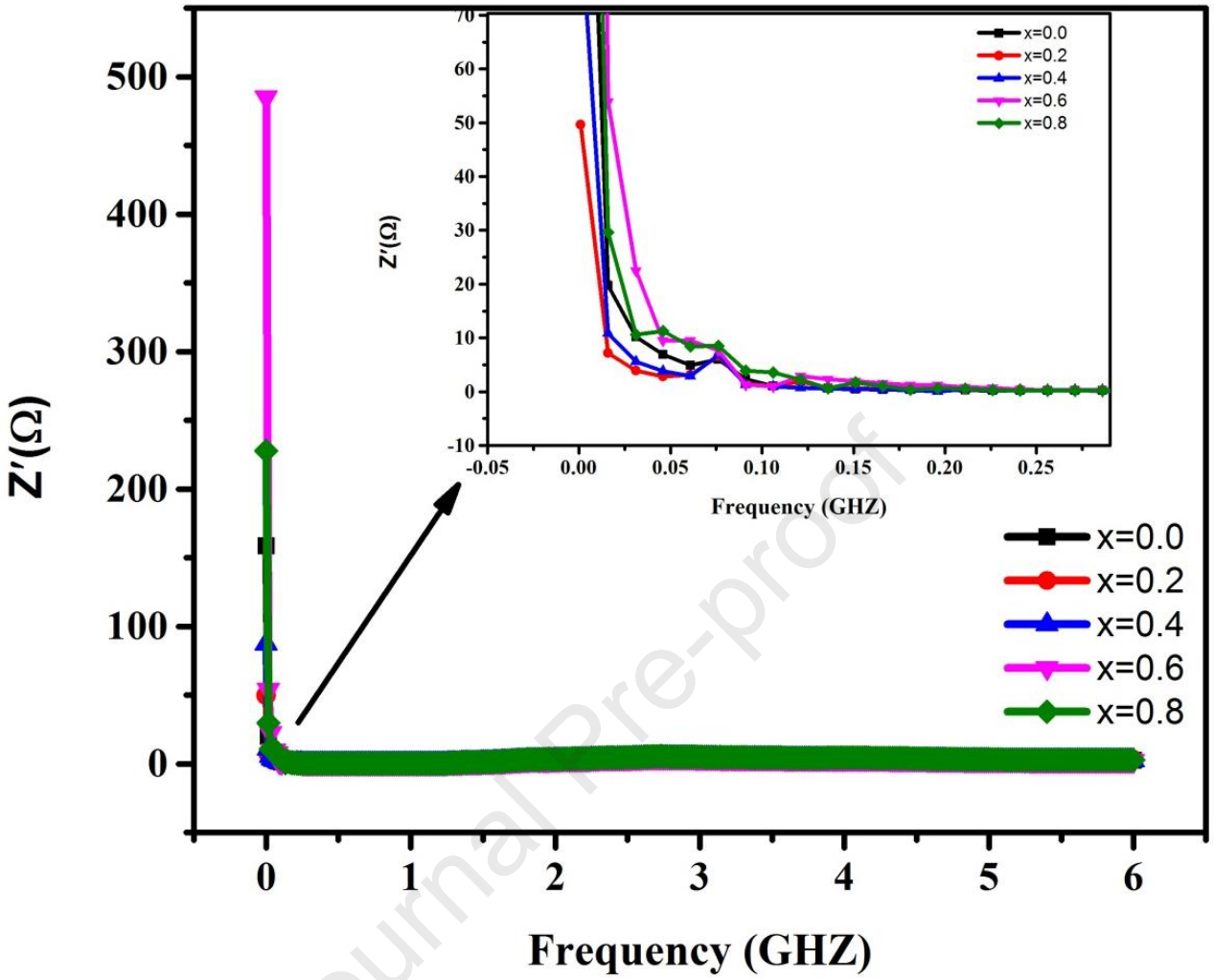

Fig. 18. The variation in Z' versus frequency of $Sr_2Ni_2Ga_xFe_{12-x}O_{22}$ ($0.00 \leq x \leq 0.8$ and $\Delta x = 0.2$) Y-type hexaferrites.

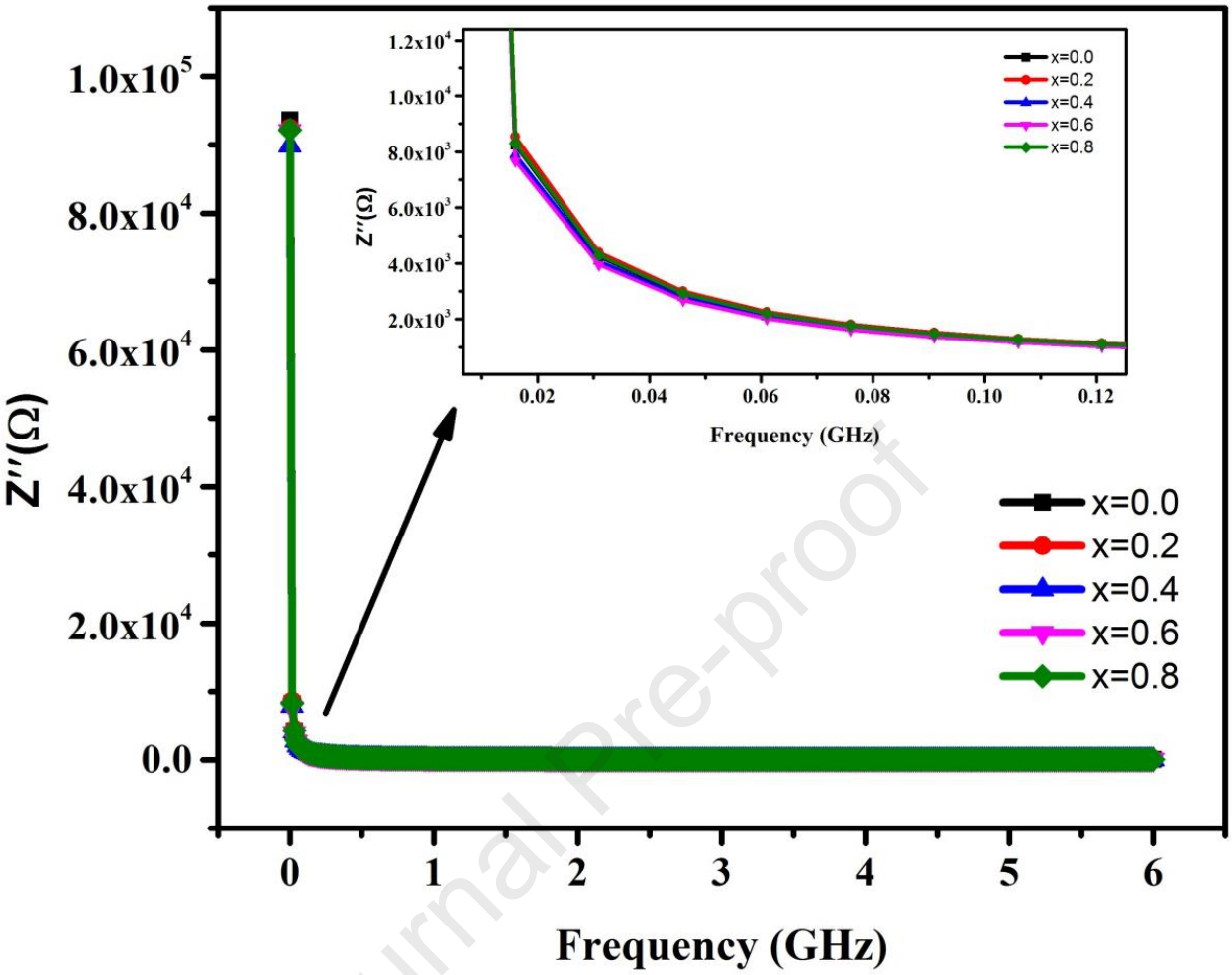

Fig. 19. The variation in Z'' versus frequency of $Sr_2Ni_2Ga_xFe_{12-x}O_{22}$ ($0.00 \leq x \leq 0.8$ and $\Delta x = 0.2$) Y-type hexaferrites.

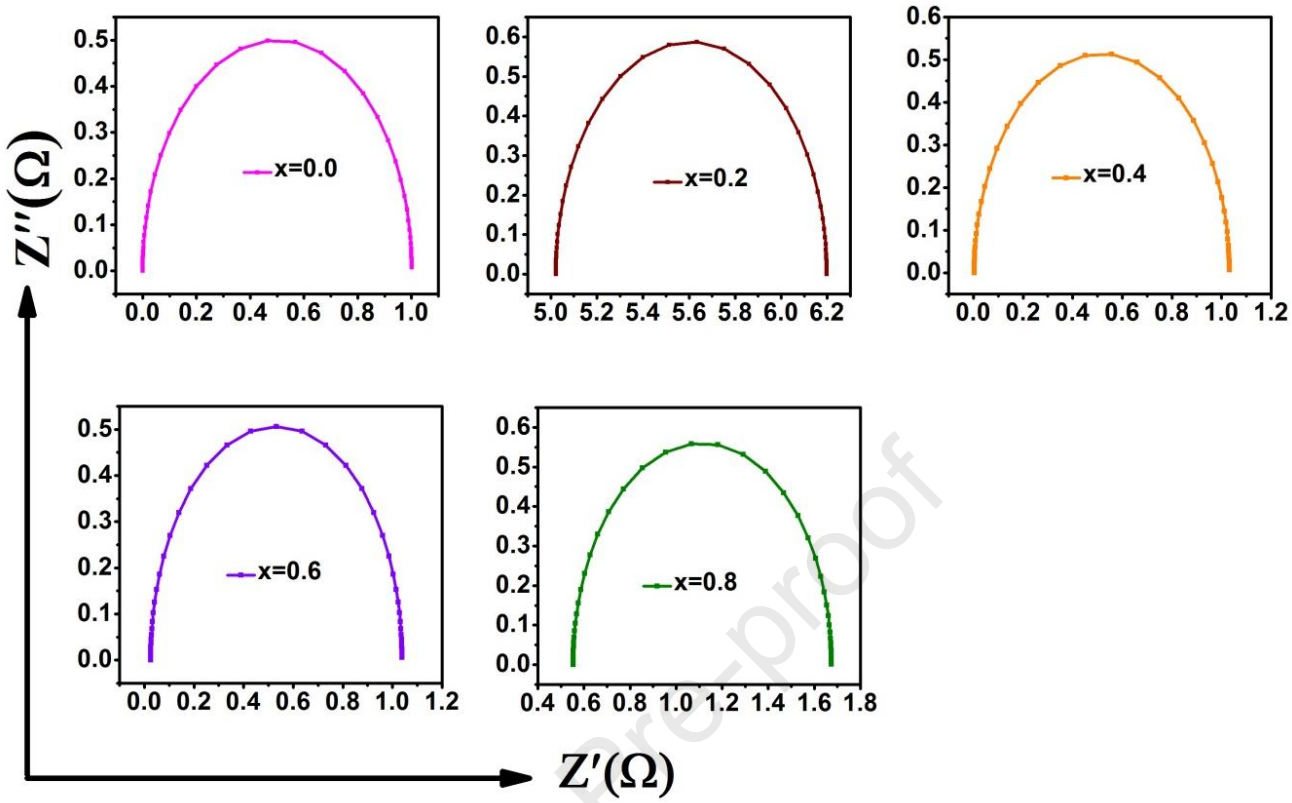

Fig. 20. Cole-Cole plot of $Sr_2Ni_2Ga_xFe_{12-x}O_{22}$ ($0.00 \leq x \leq 0.8$ and $\Delta x = 0.2$) Y-type hexaferrites.

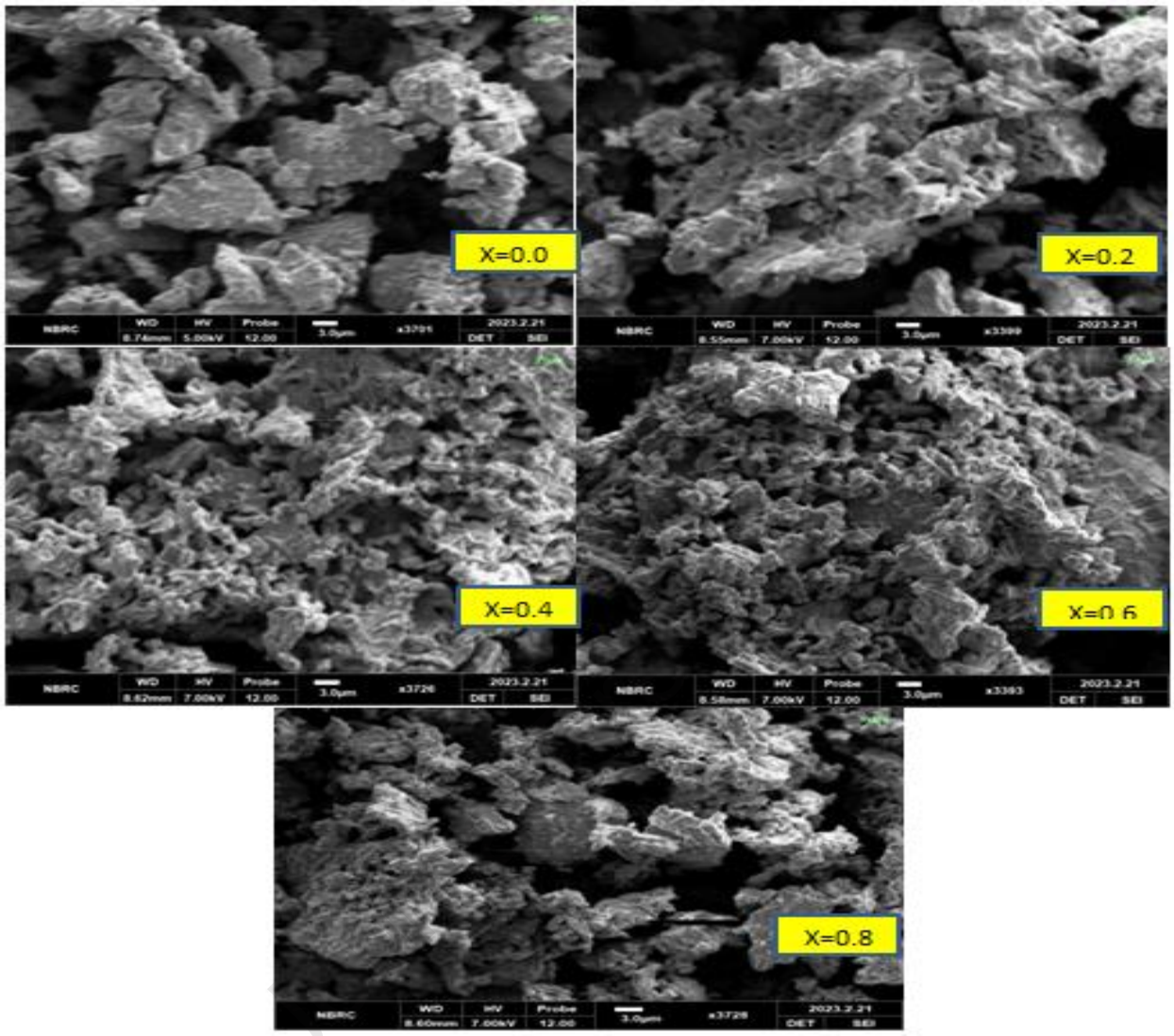

Fig. 21. SEM micrographs of $Sr_2Ni_2Ga_xFe_{12-x}O_{22}$ ($0.00 \leq x \leq 0.8$ and $\Delta x = 0.2$) Y-type hexagonal ferrites.

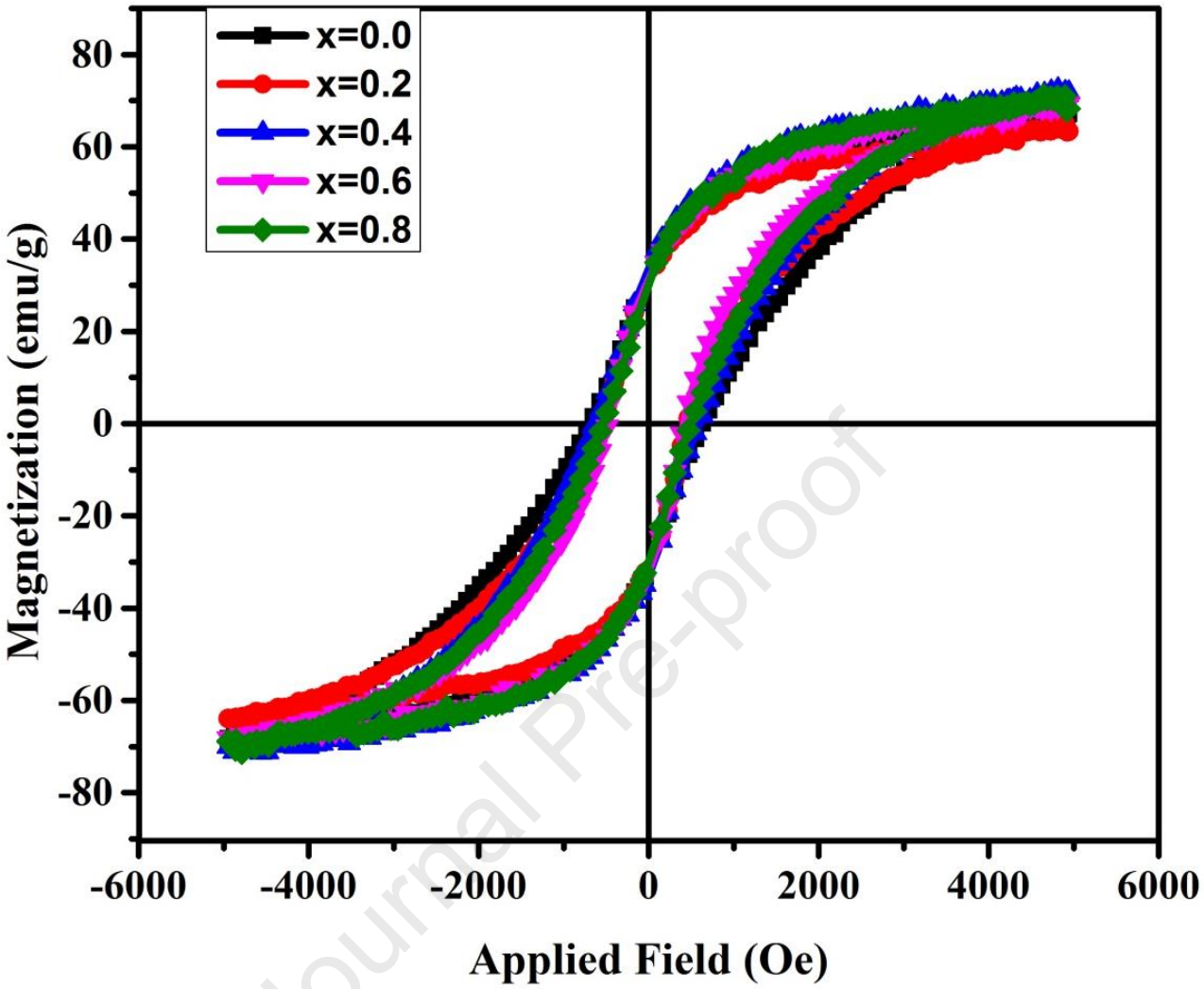

Fig. 22. Hysteresis loops of $Sr_2Ni_2Ga_xFe_{12-x}O_{22}$ (x=0.00, 0.2, 0.4, 0.6 and 0.8) Y-type hexagonal ferrites.

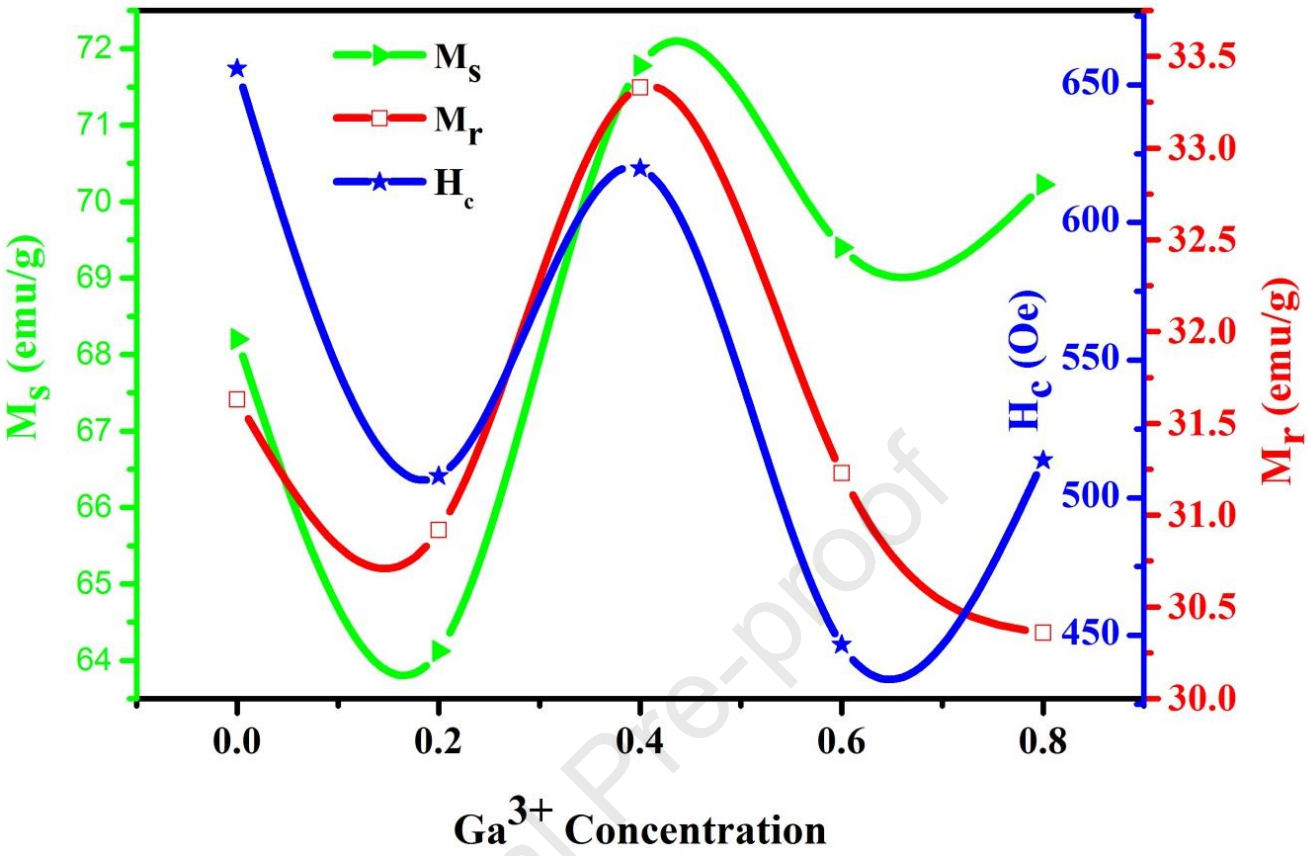

Fig. 23. The variation of Ga^{3+} concentration vs magnetic parameters for $Sr_2Ni_2Ga_xFe_{12-x}O_{22}$ (x=0.00, 0.2, 0.4, 0.6 and 0.8) Y-type hexagonal ferrites.

Declaration of interests

☒ The authors declare that they have no known competing financial interests or personal relationships that could have appeared to influence the work reported in this paper.

☐The authors declare the following financial interests/personal relationships which may be considered as potential competing interests: